NEUROSCIENCE

A mammalian-specific Alex3/Gα$_q$ protein complex regulates mitochondrial trafficking, dendritic complexity, and neuronal survival

Ismael Izquierdo-Villalba[1]†‡, Serena Mirra[2,3,4,5,6]†, Yasmina Manso[2,4]†, Antoni Parcerisas[2,4,7], Javier Rubio[1], Jaume Del Valle[4,8], Francisco J. Gil-Bea[4,9], Fausto Ulloa[2,4], Marina Herrero-Lorenzo[2], Ester Verdaguer[2,4], Cristiane Benincá[1]§, Rubén D. Castro-Torres[2], Elena Rebollo[1], Gemma Marfany[3,5,6], Carme Auladell[2,4], Xavier Navarro[4,8], José A. Enríquez[10,11], Adolfo López de Munain[4,9,12], Eduardo Soriano[2,4]*¶, Anna M. Aragay[1]*¶

Mitochondrial dynamics and trafficking are essential to provide the energy required for neurotransmission and neural activity. We investigated how G protein–coupled receptors (GPCRs) and G proteins control mitochondrial dynamics and trafficking. The activation of Gα$_q$ inhibited mitochondrial trafficking in neurons through a mechanism that was independent of the canonical downstream PLCβ pathway. Mitoproteome analysis revealed that Gα$_q$ interacted with the Eutherian-specific mitochondrial protein armadillo repeat–containing X-linked protein 3 (Alex3) and the Miro1/Trak2 complex, which acts as an adaptor for motor proteins involved in mitochondrial trafficking along dendrites and axons. By generating a CNS-specific Alex3 knockout mouse line, we demonstrated that Alex3 was required for the effects of Gα$_q$ on mitochondrial trafficking and dendritic growth in neurons. Alex3-deficient mice had altered amounts of ER stress response proteins, increased neuronal death, motor neuron loss, and severe motor deficits. These data revealed a mammalian-specific Alex3/Gα$_q$ mitochondrial complex, which enables control of mitochondrial trafficking and neuronal death by GPCRs.

INTRODUCTION

Mitochondria play a key role in producing the energy necessary for cell function and survival. In neurons, mitochondria are essential to provide the high energy supply needed for neurotransmission and neuronal activity. To fulfill this role, neuronal mitochondria are transported along dendritic and axonal projections through a complex with the motor proteins kinesin and dynein, the atypical Rho-like guanosine triphosphatases (GTPases) Miro1 and Miro2, and several adaptors including trafficking kinesin proteins (Trak1/2) (*1*–*3*). Ca^{2+}-dependent neuronal activity drives disassembly of this complex, causing local mitochondrial arrest at sites of high neuronal activity and energy demand (*4*–*6*). Consistent with this important role in neurons, alterations in mitochondrial trafficking are associated with neurodegenerative disorders (*7*–*11*).

The *ARMCX3* gene belongs to the *GPRASP* [G protein–coupled receptor (GPCR)–associated sorting protein]/*ARMCX* (armadillo repeat–containing proteins on the X chromosome) family, a Eutherian-exclusive genomic cluster located in chromosome X, which originated by retrotransposition of the ancestral *ARMC10* gene (*12*–*14*). Whereas mutations in members of the *GPRASP* subfamily are associated with delayed pulmonary development and psychiatric and intellectual disabilities (*12*), mutations in *ARMCX* subfamily genes are related to tumor progression (*14*, *15*). The *Armcx3* and *Armc10* genes are highly expressed in neurons, and the protein products localize to mitochondria and regulate mitochondrial trafficking through their interaction with the Miro/Trak complex in a Ca^{2+}-dependent manner (*14*, *16*). In addition, ARMCX is necessary for axonal regeneration (*17*).

GPCR signaling occurs not only at the plasma membrane but also at intracellular membranes (*18*, *19*). In particular, GPCRs and G proteins are integral components of mitochondria (*19*, *20*), where they control cellular respiration and energy production in addition to mitochondrial trafficking and cognition (*21*–*23*). The effects of intracellular GPCR and G proteins may be different from signals activated by surface proteins and may modulate mitochondrial-specific signaling pathways. The Gα$_q$ protein subfamily is abundant in the nervous system and is localized to the outer and inner mitochondrial membrane (*20*, *24*). This subfamily mediates the signaling of important neuronal metabotropic receptors (such as type I glutamatergic and cholinergic muscarinic receptors) and is involved in various physiological processes including motor functions, learning, and memory (*25*–*27*). In mitochondria, Gα$_q$ regulates morphology and

[1]Institut de Biologia Molecular de Barcelona (IBMB-CSIC), Barcelona 08028, Spain. [2]Department of Cell Biology, Physiology and Immunology, and Institute of Neurosciences, University of Barcelona, Barcelona 08028, Spain. [3]Department of Genetics, Microbiology and Statistics, University of Barcelona, Barcelona 08028, Spain. [4]Centro de Investigación Biomédica en Red sobre Enfermedades Neurodegenerativas (CIBER-CIBERNED), ISCIII, Madrid 28031, Spain. [5]Centro de Investigación Biomédica en Red sobre Enfermedades Raras (CIBER-CIBERER), ISCIII, Madrid 28031, Spain. [6]Institut de Biomedicina- Institut de Recerca Sant Joan de Déu (IBUB-IRSJD), Universitat de Barcelona, Barcelona 08028, Spain. [7]Biosciences Department, Faculty of Sciences, Technology and Engineering, University of Vic, Central University of Catalonia (UVic-UCC); and Tissue Repair and Regeneration Laboratory (TR2Lab), Institut de Recerca i Innovació en Ciències de la Vida i de la Salut a la Catalunya Central (IRIS-CC), 08500 Vic, Spain. [8]Department of Cell Biology, Physiology and Immunology, and Institute of Neurosciences, Universitat Autonoma de Barcelona, Bellaterra, Barcelona 08193, Spain. [9]Neurosciences Area, Biodonostia Health Research Institute, San Sebastián 20014, Spain. [10]Fundación Centro Nacional de Investigaciones Cardiovasculares Carlos III, Madrid 28029, Spain. [11]Centro de Investigación Biomédica en Red en Fragilidad y Envejecimiento Saludable (CIBER-CIBERFES), Madrid 28031, Spain. [12]Neurology Department, Donostia University Hospital, San Sebastián 20014, Spain.
*Corresponding author. Email: aarbmc@ibmb.csic.es (A.M.A.); esoriano@ub.edu (E.S.)
†These authors contributed equally to this work.
‡Present address: Kirby Neurobiology Center, Boston Children's Hospital, Boston, MA 02115, USA.
§Present address: Department of Medicine, Endocrinology, David Geffen School of Medicine, University of California, Los Angeles, CA 90095, USA.
¶These authors contributed equally to this work.

oxidative phosphorylation (OXPHOS) activity (*24*), but the molecular mechanisms involved are not understood. Here, we revealed a mechanism for $G\alpha_q$ as a component of the mitochondrial motility machinery, with armadillo repeat–containing X-linked protein 3 (Alex3) as a direct binding partner. Together, they controlled mitochondrial distribution and trafficking, dendritic complexity, synapse formation, and neuronal survival, thereby revealing a mitochondrial regulatory mechanism specific to mammals that may be important for higher brain functions.

RESULTS

$G\alpha_q$ regulates mitochondrial trafficking in neurons

To investigate the role of $G\alpha_q$ in axonal mitochondrial trafficking, we used designer receptors exclusively activated by designer drugs (DREADD). Hippocampal mouse neurons were cotransfected at 4 days in vitro (DIV) with mitochondrial–green fluorescent protein (mitoGFP) and the mCherry-hM3Dq DREADD-$G\alpha_q$ receptor (*28*, *29*), which was detected along the axons, dendrites, and cell bodies (Fig. 1A). Two days later, mitochondria were imaged in axonal segments located 90- to 160-μm distal to the soma (fig. S1A), before and after addition of the DREADD ligand clozapine N-oxide (CNO) (Fig. 1, B and C). Ligand stimulation reduced bidirectional mitochondrial motility and the percentage of time in motion in both the anterograde and retrograde directions. There was a nonsignificant increase in the number of stops per mitochondrion (Fig. 1C).

The impact of $G\alpha_q$ on mitochondrial motility was analyzed in hippocampal neurons transfected with cytosolic GFP and bicistronic vectors encoding mitoDsRed and either the constitutively active mutant $G\alpha_q$R183C or the wild-type (WT) form of $G\alpha_q$ (fig. S1B). Expression of $G\alpha_q$R183C reduced anterograde and retrograde mitochondrial trafficking and the percentage of motile mitochondria and increased the number of stops per mitochondrion without altering transport velocities (Fig. 1, D and E, and fig. S1C). In contrast, expression of WT $G\alpha_q$ increased anterograde transport and reduced retrograde trafficking (Fig. 1, D and E).

The involvement of phospholipase Cβ (PLCβ), the canonical $G\alpha_q$ effector, was evaluated using a form of $G\alpha_q$ with mutations at critical residues (R156 and T257) in the effector region. This mutant has been used to study the contribution of the noncanonical effects of $G\alpha_q$ because it still binds to guanosine 5′-triphosphate (GTP) but not to PLCβ (*30*–*32*). Expression of the GFP-$G\alpha_q$R183C/R156A/T257A (RCAA) mutant (with the constitutively activating R183C mutation and the R156A and T257A mutations to block PLCβ binding) led to an arrest of mitochondrial trafficking similar to that observed with expression of GFP-$G\alpha_q$R183C (Fig. 1, F to H). In contrast, expression of the N terminus of $G\alpha_q$ (GFP-NT; amino acids 1 to 142) did not produce changes relative to control conditions (fig. S1, D to F). Treatment with the inositol 1,4,5-trisphosphate (IP3) receptor antagonist xestospongin C (*33*, *34*) did not alter $G\alpha_q$-mediated effects, further suggesting that the $G\alpha_q$-induced mitochondrial trafficking effects were independent of activation of the PLCβ pathway (fig. S1, G and H).

We used the potent and selective $G\alpha_q$ inhibitor YM-254890 to further support the specific role of $G\alpha_q$ in these mitochondrial trafficking effects (*35*, *36*). YM-254890 treatment rescued the retrograde transport and the differences in the number of stops upon expression of the constitutively active $G\alpha_q$R183C (fig. S2, A and B). In contrast, synaptic vesicle traffic was not affected by $G\alpha_q$ expression, suggesting that $G\alpha_q$ effects on trafficking may be specific to mitochondria (Fig. 1I and fig. S2C). No differences were observed in the staining pattern for the membrane potential–sensitive MitoTracker Red CMXRos in human embryonic kidney (HEK) 293 cells and neurons expressing GFP-$G\alpha_q$ or the different mutant forms of GFP-$G\alpha_q$ (Fig. 1, J and K, and fig. S2, D and E), suggesting that the effects of $G\alpha_q$ or $G\alpha_q$R183C expression were independent of mitochondrial membrane potential.

To further analyze the effect of $G\alpha_q$ in mitochondrial trafficking, we knocked down $G\alpha_q$ ($G\alpha_q$ KD) using specific short hairpin RNAs (fig. S2, F and G). Reducing $G\alpha_q$ levels increased retrograde mitochondrial transport and the percentage of motile mitochondria, concomitant with a decrease in mitochondrial stops (fig. S2, H and I), which further supports the involvement of $G\alpha_q$ in regulating mitochondrial motility. Together, these findings suggest that $G\alpha_q$ activation induces mitochondrial arrest, whereas an increase in $G\alpha_q$ levels enhances anterograde movement and the absence of $G\alpha_q$ increases the number of motile mitochondria.

$G\alpha_q$ interacts specifically with the armadillo domain of Alex3

We next sought to identify binding partners of $G\alpha_q$ that could be involved in the control of mitochondrial dynamics. $G\alpha_q$ immunoprecipitates from mitochondrial- enriched membranes from WT mouse embryonic fibroblasts (MEFs), MEFs deficient in $G\alpha_q$ and Gα11 ($G\alpha_q$ KO), and $G\alpha_q$ KO MEFs with $G\alpha_q$ expression ($G\alpha_q$ KO + $G\alpha_q$), and NIH 3T3 cells were subjected to mass spectrometry (MS) analysis. Extracts of membranes from $G\alpha_q$ KO MEFs (*24*) were used as controls. The $G\alpha_q$ mitoproteome included the mitochondrial trafficking protein Alex3, which had many peptides identified (22 peptides in three cell lines) (fig. S3A). Alex3 belongs to the GPRASP/ARMCX family, which includes some GPCR-interacting members, and the ARMCX subfamily is expressed in the nervous system of Eutherian mammals (*12*, *13*).

The MS results were validated in brain homogenates, in SHSY5Y and MEF extracts immunoprecipitated with different antibodies directed against either Alex3 or $G\alpha_q$ (Fig. 2, A and B, and fig. S3B), and in cells expressing the constitutively active mutant $G\alpha_q$R183C and either Myc- or GFP-tagged Alex3 (fig. S3, C to E). In contrast, Gβγ, which is present at mitochondria (*37*), did not immunoprecipitate with Myc-Alex3 (fig. S3F). Further, pull-down experiments using GFP-tagged truncated Alex3 proteins showed that the region of interaction was the proximal armadillo domain of Alex3 (Fig. 2, C and D, and fig. S3, G to I) (*38*). Last, we used purified $G\alpha_q$ protein (*39*) to probe the direct interaction with both the full-length and C terminus of glutathione *S*-transferase (GST)–Alex3 in the presence of guanosine diphosphate (GDP) (Fig. 2, E and F). Overall, these results confirmed a direct interaction between $G\alpha_q$ and the proximal region of the armadillo domain of Alex3.

To address whether Alex3 was a putative effector of $G\alpha_q$, we compared the binding to the constitutively active mutants of $G\alpha_q$, $G\alpha_q$R183C (RC) and $G\alpha_{qQ}$209L (QL). $G\alpha_q$R183C has reduced *k*cat for GTP hydrolysis but still depends on guanine nucleotide exchange factor (GEF) for its activity, whereas $G\alpha_q$Q209L binds directly to effectors in the absence of GEF activation. Alex3 showed reduced immunoprecipitation with $G\alpha_q$Q209L compared with $G\alpha_q$R183C (Fig. 2G). Moreover, Alex3 immunoprecipitated with the $G\alpha_q$Q209L/R256A/T257A (QLAA) mutant, which cannot bind to PLCβ (Fig. 2G) (*30*, *32*). Consistently, expression of GRK2 (a GPCR-specific kinase that binds to $G\alpha_q$ at the canonical effector domain) did not diminish the Alex3/$G\alpha_q$ interaction (Fig. 2H) (*40*).

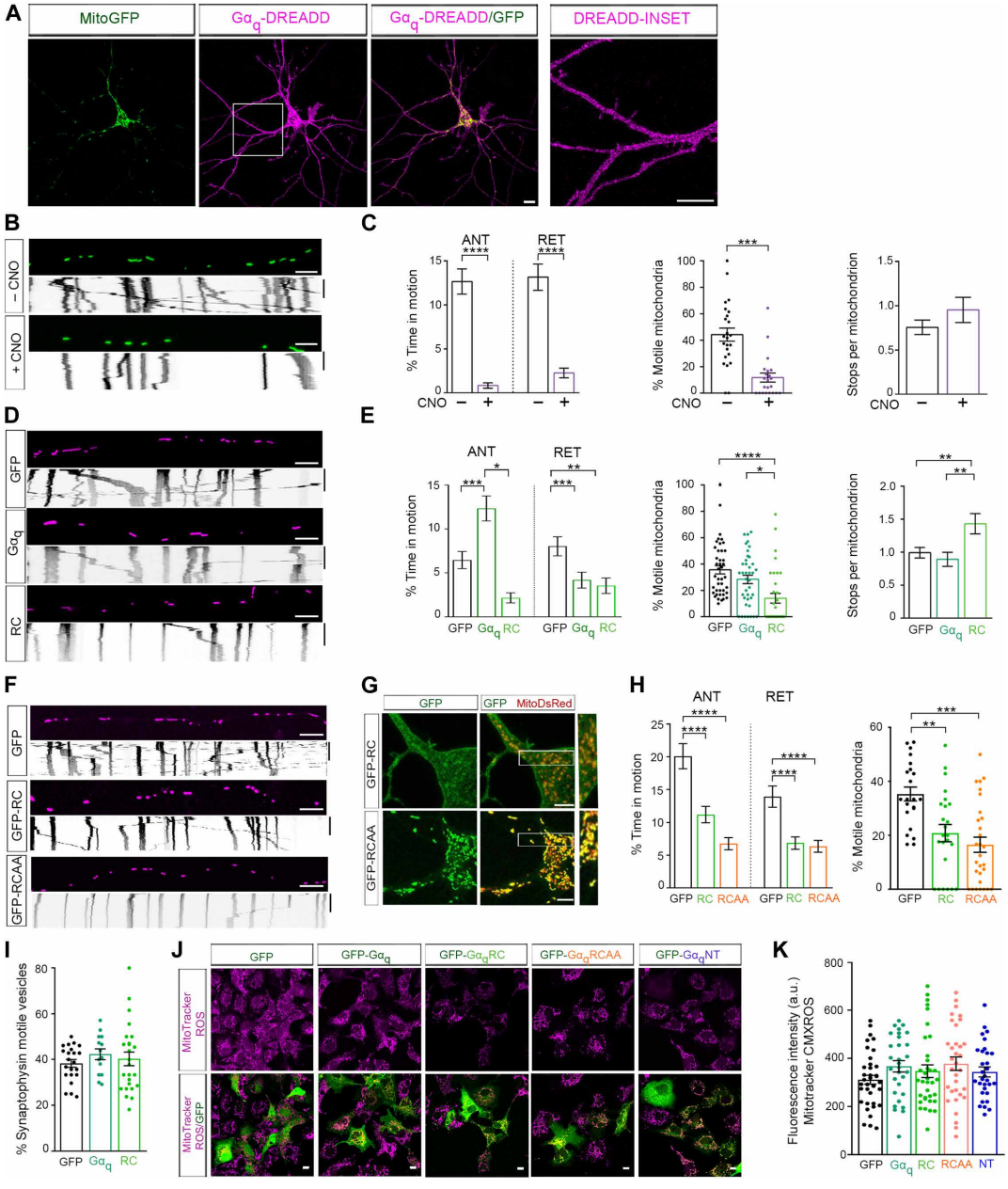

Fig. 1. Gα$_q$ regulates mitochondrial motility in axons. (**A**) Confocal images from hippocampal neurons expressing mitoGFP and the Gα$_q$-specific hM3D-DREADD-Cherry receptor (Gα$_q$-DREADD). (**B**) Images and kymographs from axons expressing mitoGFP and Gα$_q$-DREADD before (−CNO) or after the addition of CNO (+CNO). Images show axonal mitochondria at $t = 0$ and corresponding kymographs over a 10-min period (y axis). (**C**) Bar graphs showing the percentage of time in motion in the anterograde (ANT) and retrograde (RET) directions, percentage of motile mitochondria, and stops per mitochondrion from images as in (B). $n = 387$ (−CNO) and 429 (+CNO) total mitochondria from 24 and 22 axons, respectively, from $n = 6$ to 9 mouse embryos analyzed in three independent experiments. (**D**) Images and kymographs from axons expressing GFP and mitoDsRed without (GFP) or with WT Gα$_q$ or Gα$_q$R183C (RC). (**E**) Bar graphs showing the percentage of time in motion, percentage of motile mitochondria, and stops per mitochondria from images as in (D). $n = 470$ (GFP), 390 (Gα$_q$), and 305 (RC) total mitochondria from 42, 39, and 33 different axons, respectively, from $n = 8$ to 12 mouse embryos analyzed in four independent experiments. (**F**) Images and kymographs from axons expressing mitoDsRed with GFP, GFP-Gα$_q$R183C (GFP-RC), or GFP-Gα$_q$R183C/R156A/T257A (GFP-RCAA). (**G**) Representative immunofluorescent images from neurons expressing GFP and mitoDsRed as in (F). (**H**) Bar graphs showing the percentage of time in motion and percentage of motile mitochondria from images as in (F). $n = 336$ (GFP), 500 (RC), and 569 (RCAA) mitochondria from $n = 22$, 24, and 29 different axons, respectively, from $n = 6$ to 9 mouse embryos analyzed in three independent experiments. (**I**) Quantification of GFP-tagged synaptophysin$^+$ vesicles in axons expressing mitoDsRed (GFP) with or without WT Gα$_q$ (Gα$_q$) or Gα$_q$R183C (RC). $n = 22$ (GFP), 14 (Gα$_q$), and 25 (RC) axons from $n = 4$ or 5 mouse embryos analyzed in four independent experiments. See fig. S2C for corresponding images. (**J**) Representative images from HEK293 cells expressing GFP, GFP-Gα$_q$, GFP-Gα$_q$R183C (RC), GFP-Gα$_q$R183C R156A/T257A (RCAA), and GFP-Gα$_q$-NT (NT) and labeled with MitoTracker Red CMXRos. (**K**) Fluorescence intensity from images as in (J). $n = 37$ (GFP), 31 (Gα$_q$), 35 (RC), 33 (RCAA), and 29 (NT) HEK293 cells from $n = 6$ biological replicates analyzed in three independent experiments. a.u., arbitrary units. Scale bars, 10 μm (A and J) and 5 μm (B, D, F, and G). Time bars, 300 s. Data are means ± SEM. Statistical analysis: Mann-Whitney U test for (C) and Kruskal-Wallis with Dunn's multiple comparison test for (E) to (G), (I), and (K). *$P < 0.05$, **$P < 0.01$, ***$P < 0.001$, and ****$P < 0.0001$.

We found that the levels of Alex3 were decreased in $G\alpha_q$ KO MEFs (Fig. 2, I and J). We have previously shown that Wnt, a ligand for the Frizzled family of GPCR receptors, protects Alex3 from protein degradation through the canonical PLCβ–protein kinase C (PKC) axis (*33*). Together, our results indicate that Alex3 preferentially binds to the nonactive or transitional state of $G\alpha_q$ in a region distinct from canonical effectors and that $G\alpha_q$ activity maintains Alex3 levels.

$G\alpha_q$ interacts with Alex3, Miro1, and Trak2

Given that Alex3 interacts with the mitochondrial Rho GTPase Miro1 (*14*), we investigated whether $G\alpha_q$ interacted with Miro1 as well (*14*). Immunoprecipitation of Myc-Miro1 contained $G\alpha_q$ or $G\alpha_q$R183C together with endogenous Alex3 (Fig. 3A). Pull-down experiments of GST-Miro1 from SHSY5Y cell lysates demonstrated the interaction of Miro1 with endogenous $G\alpha_q$ (Fig. 3B). Miro1 is a Ca^{2+}-binding protein whose interaction with Alex3 is disrupted by high Ca^{2+} levels (*14*, *41*). The presence of high (2 mM) Ca^{2+} levels did not disrupt the coassociation between $G\alpha_q$ and Miro1, as it did with the Alex3/Miro1 interaction (Fig. 3C), suggesting that $G\alpha_q$ could remain bound to Miro1 after Alex3 dissociation.

To support the above findings, we performed confocal microscopy in Cos-7 cells and neurons (Fig. 3, D to I, and fig. S4, A to C). First, we

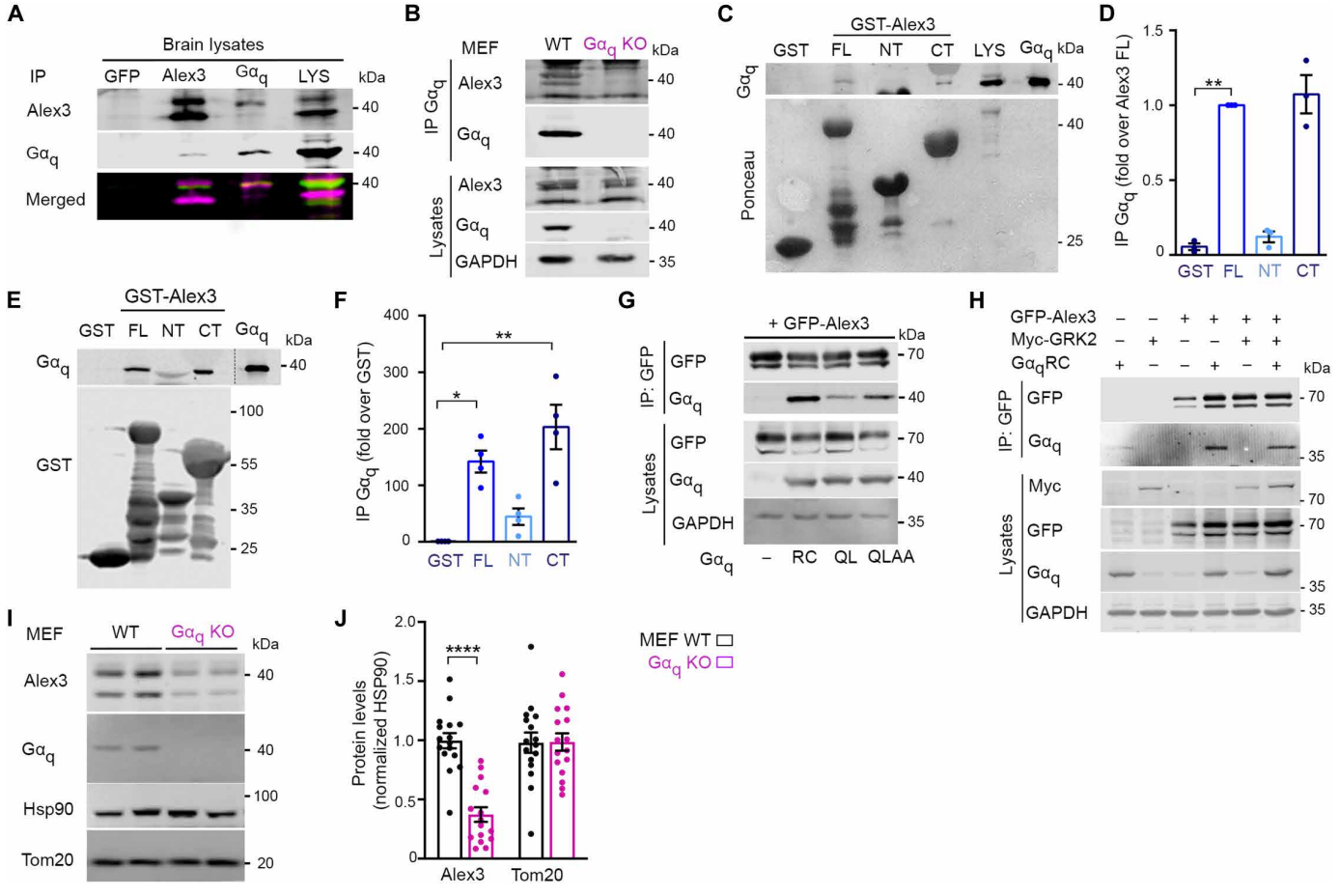

Fig. 2. $G\alpha_q$ interacts with Alex3 through its armadillo domains. (**A**) Mouse brain homogenates (LYS) were immunoprecipitated (IP) for endogenous Alex3, $G\alpha_q$, and GFP (as control). Immunoprecipitates were immunoblotted for GFP, Alex3 (magenta), and $G\alpha_q$ (green). $n = 3$ biological replicates analyzed in three independent experiments. (**B**) Endogenous $G\alpha_q$ immunoprecipitates from WT MEFs (WT) and *$G\alpha_q$/11*$^{-/-}$ MEFs ($G\alpha_q$ KO) were immunoblotted for $G\alpha_q$, Alex3, and GAPDH. $n = 3$ biological replicates per group analyzed in three independent experiments. (**C**) Pull-downs of GST, GST-tagged Alex3 full-length (FL), GST-tagged Alex3 1 to 106 (NT), or GST-tagged Alex3 107 to 379 (CT) from SHSY5Y lysates were immunoblotted for $G\alpha_q$. The $G\alpha_q$ and LYS immunoblots show purified $G\alpha_q$ protein and cell homogenates, respectively. Ponceau staining is shown. (**D**) Quantification from (C) presented as fold change relative to $G\alpha_q$ precipitated with GST-Alex-FL. $n = 3$ biological replicates analyzed in three independent experiments. (**E**) Pull-downs of purified components either with GST alone or with GST-Alex3 FL, GST-Alex3 NT, or GST-Alex3 CT (10 μg) in the presence of $G\alpha_q$ were immunoblotted for $G\alpha_q$ and GST. $G\alpha_q$ immunoblot shows purified $G\alpha_q$ protein. (**F**) Quantification from (E) represented as fold change relative to $G\alpha_q$ under the control (GST) condition. $n = 4$ biological replicates analyzed in four independent experiments. (**G**) GFP immunoprecipitates and lysates from HEK293 cells expressing GFP-Alex3 with $G\alpha_q$R183C (RC), $G\alpha_q$Q209L (QL), or $G\alpha_q$Q209L/R256A/T257A (QLAA) were immunoblotted for GFP, $G\alpha_q$, and GAPDH. $n = 4$ biological replicates per group analyzed in four independent experiments. (**H**) GFP immunoprecipitates and lysates from HEK293 cells expressing GFP-Alex3 and $G\alpha_q$R183C with or without Myc-GRK2 immunoblotted for $G\alpha_q$, GFP, and GAPDH. $n = 3$ biological replicates per group analyzed in three independent experiments. (**I**) WT and *$G\alpha_q$/11*$^{-/-}$ ($G\alpha_q$ KO) MEF lysates were immunoblotted for Alex3, Hsp90, $G\alpha_q$, and Tom20. (**J**) Quantification of (I) normalized to Hsp90 from $n = 12$ biological replicates per group analyzed in four independent experiments. Data are means ± SEM. Statistical analyses: Kruskal-Wallis with Dunn's multiple comparison test for (D) and (F) and one-way ANOVA with Bonferroni post hoc test for (J). $^*P < 0.05$, $^{**}P < 0.01$, and $^{****}P < 0.0001$.

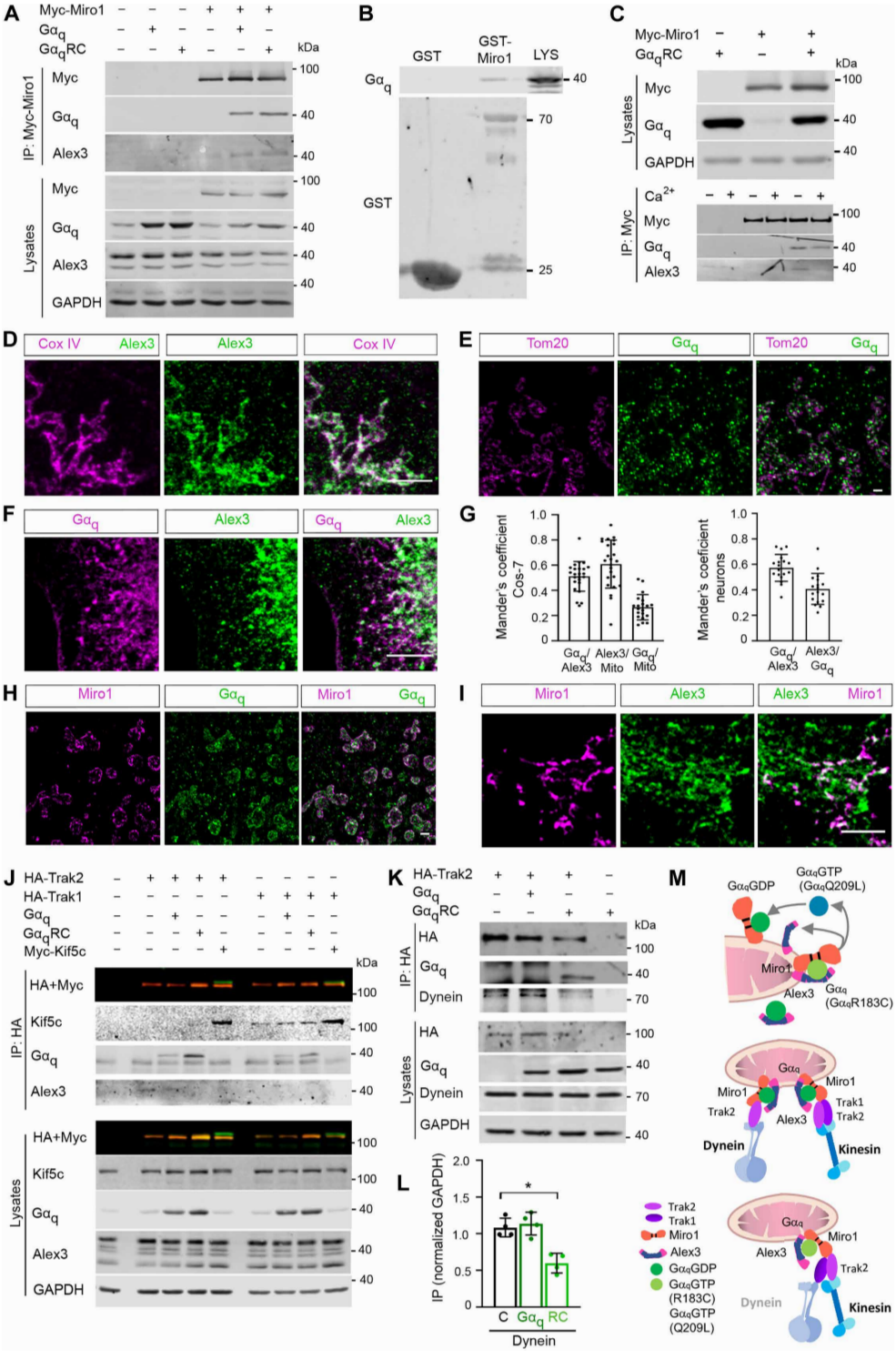

Fig. 3. $G\alpha_q$ interacts with Miro1 and Trak2. (**A**) Myc immunoprecipitates and lysates from HEK293 cells expressing Myc-Miro1 with endogenous $G\alpha_q$ ($G\alpha_q$) or $G\alpha_q$R183C ($G\alpha_q$RC) were immunoblotted for $G\alpha_q$, Alex3, GAPDH, and Myc. $n = 3$ biological replicates analyzed in three independent experiments. (**B**) GST-Miro1 pulldowns from SHSY5Y cell extracts (LYS) were immunoblotted for endogenous $G\alpha_q$ and GST. $n = 3$ biological replicates analyzed in three independent experiments. (**C**) Myc immunoprecipitates and lysates from HEK293 cells expressing Myc-Miro1 with WT $G\alpha_q$ ($G\alpha_q$) or $G\alpha_q$R183C ($G\alpha_q$RC) were immunoblotted for $G\alpha_q$, Myc, Alex3, and GAPDH. Immunoprecipitation was carried out in the presence (+) or absence (−) of 2 mM Ca^{2+}. $n = 3$ biological replicates analyzed in three independent experiments. (**D** and **E**) Confocal images of Cos-7 cells expressing exogenous $G\alpha_q$ and stained for $G\alpha_q$, Alex3, and mitochondrial markers Cox IV or Tom20-Cherry. $n = 4$ biological replicates analyzed in two independent experiments. (**F**) Confocal images of Cos-7 cells expressing exogenous $G\alpha_q$ and stained for Alex3 and $G\alpha_q$. $n = 6$ biological replicates analyzed in three independent experiments. (**G**) Mander's coefficient of colocalization was determined between $G\alpha_q$ and Alex3 ($G\alpha_q$/Alex3), Alex3 and MitoTracker Red CMXRos (Alex3/Mito), and $G\alpha_q$ and MitoTracker Red CMXRos ($G\alpha_q$/Mito) from images of Cos-7 cells transfected with $G\alpha_q$ and stained for Alex3 or from images of hippocampal neurons (4 to 5 DIV) transfected with $G\alpha_q$ and stained for Alex3. $n = 24$ Cos-7 cells for $G\alpha_q$/Alex3 and Alex3/Mito and $n = 20$ Cos-7 cells for $G\alpha_q$/Mito from $n = 6$ biological replicates analyzed in three independent experiments. $n = 18$ neurons from $n = 3$ mouse embryos analyzed in three independent experiments. Corresponding images are shown in fig. S4 (A and B). (**H**) Confocal super-resolution images of Cos-7 cells expressing Miro1-Cherry and exogenous $G\alpha_q$ stained for $G\alpha_q$. See fig. S4 (C and D) for more examples of images and mitochondria line profiles. $n = 2$ biological replicates per group analyzed in two independent experiments. (**I**) Confocal images of Cos-7 cells expressing Miro1-GFP and stained for Alex3. Images were taken using the Zeiss LSM780 (D, F, and I) and Nikon *N*-SIM (H and E) high-resolution confocal microscopes. $n = 3$ biological replicates per group analyzed in three independent experiments. (**J**) HA immunoprecipitates and lysates from HEK293 cells expressing HA-Trak1, HA-Trak2, WT $G\alpha_q$ ($G\alpha_q$), $G\alpha_q$R183C ($G\alpha_q$RC), and/or Myc-Kif5c were immunoblotted for HA, Myc, $G\alpha_q$, Alex3, and GAPDH. $n = 3$ biological replicates per group analyzed in three independent experiments. (**K**) HA immunoprecipitates and lysates from HEK293 cells expressing HA-Trak2, WT $G\alpha_q$ ($G\alpha_q$), or $G\alpha_q$R183C ($G\alpha_q$RC) were immunoblotted for endogenous dynein (Dynein), $G\alpha_q$, HA-Trak2, and GAPDH. (**L**) Quantification from (K) normalized to GAPDH from $n = 4$ biological replicates analyzed in four independent experiments. (**M**) Models of the interaction between $G\alpha_q$, Alex3, Miro1, and Trak1/2. $G\alpha_q$ associates with Alex3 and Miro1 in its GDP-bound form and in its transitional state ($G\alpha_q$R183C). Alex3 dissociates from Miro1 upon increases in Ca^{2+} and from $G\alpha_q$ in the presence of the full-length, constitutively active form ($G\alpha_q$Q209L). Alex3, $G\alpha_q$, and Miro1 interact with Trak1 and Trak2. $G\alpha_q$ potentiates the binding of Trak2 to Kif5c. Scale bars, 5 μm (D to F) and 1 μm (H and I). Data are means ± SEM. Statistical analyses: One-way ANOVA with Bonferroni post hoc test for (K). $^*P < 0.05$.

confirmed the localization of $G\alpha_q$ and Alex3 within the mitochondrial network identified with either translocase of outer membrane 20 (Tom20) or cytochrome c oxidase subunit IV (Cox IV), although these proteins were also found outside this compartment (Fig. 3, D and E). Similarly, we observed colocalization between $G\alpha_q$ and Alex3 in mitochondrial-like organelles and other cytoplasmic regions both in Cos-7 cells and hippocampal neurons (Fig. 3, F and G, and fig. S4, A and B). Last, both Alex3 and $G\alpha_q$ exhibited a close localization with the mitochondrial protein Miro1 (Fig. 3, H and I, and fig. S4, C and D). Overall, these results are consistent with our biochemical experiments demonstrating an Alex3/$G\alpha_q$/Miro1 complex on mitochondria.

Miro1 and Miro2 recruit kinesin and dynein motors to mitochondria by binding to the adaptor proteins Trak1 and Trak2 (*42*). Trak1 recruits both dynein and kinesin, whereas Trak2 preferentially interacts with dynein (*43*). We analyzed the interactions of Trak1 and Trak2 with the motor protein Kif5c (kinesin family member 5C) in the presence of active $G\alpha_q$. $G\alpha_q$ immunoprecipitated with both Kif5c and Miro1 and with Trak1 or Trak2 proteins (Fig. 3J and fig. S4, E and F). Endogenous Alex3 immunoprecipitated with Trak2, as shown previously (*14*), and also in the presence of $G\alpha_q$ (Fig. 3J). Constitutively active $G\alpha_q$R183C was present in a complex with Trak2 and endogenous Kif5c (Fig. 3J)). Further, dynein binding to Trak2 was diminished in the presence of $G\alpha_q$R183C (Fig. 3, K and L), although no changes were found in the interaction of dynein with Trak1 (fig. S4G). In contrast, the GTP-active mutant $G\alpha_q$Q209L did not coassociate with Trak1, which correlated with the reduced interaction with Alex3 (Fig. 2G and fig. S4G). Together, these findings suggest that $G\alpha_q$ potentiates mitochondrial anterograde movement (Fig. 3M) by favoring the complex between Trak1/2 and kinesin concurrently with decreased dynein/Trak2 interaction and decreased Alex3 protein levels in the complex.

Central nervous system–specific inactivation of *Armcx3* demonstrates that $G\alpha_q$ effects on mitochondrial trafficking depend on Alex3

To investigate the contribution of Alex3 in $G\alpha_q$-mediated regulation of mitochondrial trafficking, we generated a central nervous system (CNS)–specific *Armcx3* KO mouse line (*Armcx3*$^{fl/fl}$/*Nestin-Cre*) (Alex3 CKO) (fig. S5A). Western blot analysis of CNS extracts from embryonic day 14 (E14) and postnatal day 5 (P5) to P7 mouse samples confirmed the absence of Alex3 in Alex3 CKO mice (Fig. 4, A to D, and fig. S5B). Alex3 CKO mice were viable at postnatal stages and exhibited normal cytoarchitectonics (Fig. 4E). Armadillo domains typically act as chaperones for Gα subunits (*44*). Here, we found that the levels of $G\alpha_q$ were reduced in the brains of Alex3 CKO mice compared with those of control littermates (fig. S5, C and D).

We evaluated the effect of *Armcx3* gene deletion on mitochondrial trafficking. Analysis of kymographs of hippocampal neurons from Alex3 CKO mice showed significant decrease in the percentage of motile mitochondria and the time in motion and an increase in the number of mitochondrial stops compared with neurons from control mice (Fig. 4, F to I). These results are consistent with previous findings showing reduced neuronal mitochondrial trafficking upon Alex3 knockdown (*14*).

To resolve the contribution of Alex3 in the regulation of mitochondrial trafficking by $G\alpha_q$, we expressed the active form of $G\alpha_q$ in Alex3 CKO hippocampal neurons. $G\alpha_q$R183C expression or *Armcx3* deletion produced the expected decrease in mitochondrial trafficking. The effects of $G\alpha_q$R183C on motile mitochondria were not observed in Alex3 CKO hippocampal neurons, suggesting a functional interaction between these proteins. Moreover, expression of constitutively active $G\alpha_q$ in Alex3 CKO neurons rescued the defect in anterograde movement (Fig. 4, J to L). These results indicate the requirement of Alex3 to sustain mitochondrial arrest by $G\alpha_q$ during anterograde transport and suggest a functional link between these proteins.

We also analyzed the effects of activating the GPCR-specific $G\alpha_q$ pathway on mitochondrial trafficking by expressing the Cherry-tagged hM3Dq DREADD-$G\alpha_q$ receptor in Alex3 CKO neurons. CNO-induced DREADD activation reduced mitochondrial trafficking to a lesser extent in the absence of Alex3 (fig. S5, E to G). Conversely, the increased mitochondrial trafficking observed upon $G\alpha_q$ knockdown was largely unaffected by the lack of Alex3 protein (fig. S5, H to J).

Although we found reduced numbers of mitochondria in Alex3 CKO neurons, mitochondrial length was not altered (fig. S5, K to M). Instead, expression of constitutively active $G\alpha_q$ or silencing of $G\alpha_q$ ($G\alpha_q$ KD) increased the number of mitochondria irrespective of Alex3 expression, and the former decreased mitochondrial length when Alex3 was present (fig. S5, N to P). Ligand activation of DREADD-$G\alpha_q$ in hippocampal neurons reduced mitochondrial size (fig. S5, Q to S). Overall, these results suggest cross-talk between $G\alpha_q$ and Alex3 in the control of mitochondrial dynamics.

Mitochondrial distribution depends on Alex3 and the activation of $G\alpha_q$

Defects in mitochondrial motility may cause altered mitochondrial distribution in dendrites and axons (*45*). We thus performed a mitochondrial distribution analysis on hippocampal neurons (Fig. 5, A and B). The Mito80 value (the location of 80% of proximal mitochondria) revealed increased mitochondrial accumulation near the soma in Alex3 CKO neurons compared with in control neurons (Fig. 5C). In contrast, expression of the constitutively active form of $G\alpha_q$ induced a redistribution of mitochondria toward the periphery of dendrites (Fig. 5D). In line with this finding, expression of constitutively active $G\alpha_q$ prevented the concentration of mitochondria near the soma in the absence of Alex3 (Fig. 5E). Next, we measured the density of mitochondria in the cell bodies of cultured neurons. The mitochondrial accumulation near cell bodies seen in Alex3 CKO neurons was partially reversed by the expression of active $G\alpha_q$ (Fig. 5F). In contrast, $G\alpha_q$ KD did not cause significant changes in mitochondrial distribution in control or Alex3 CKO neurons (fig. S6, A and B). Together, these data indicate that the absence of Alex3 results in an altered mitochondrial distribution in neurites concomitant with a mitochondrial accumulation near cell bodies, whereas activation of $G\alpha_q$ partially reverses these effects.

Alex3 and $G\alpha_q$ are required for proper dendritic arborization

We next investigated the impact of Alex3-related mitochondrial alterations in dendritic morphogenesis (Fig. 6A). Compared with control neurons, we found an overall decrease in total dendritic length in Alex3 CKO neurons, along with a higher number of primary dendrites and a lower density of branching points, which correlated with an altered Sholl analysis (Fig. 6, B and C).

Neurons expressing $G\alpha_q$R183C had fewer and less complex dendrites, an effect not seen in neurons expressing WT $G\alpha_q$ (Fig. 6, D and E). Expression of constitutively active $G\alpha_q$ R183C in Alex3 CKO neurons largely reverted the *Armcx3* deletion–induced alterations in primary dendrites (Fig. 6, F and G). The expression of $G\alpha_q$

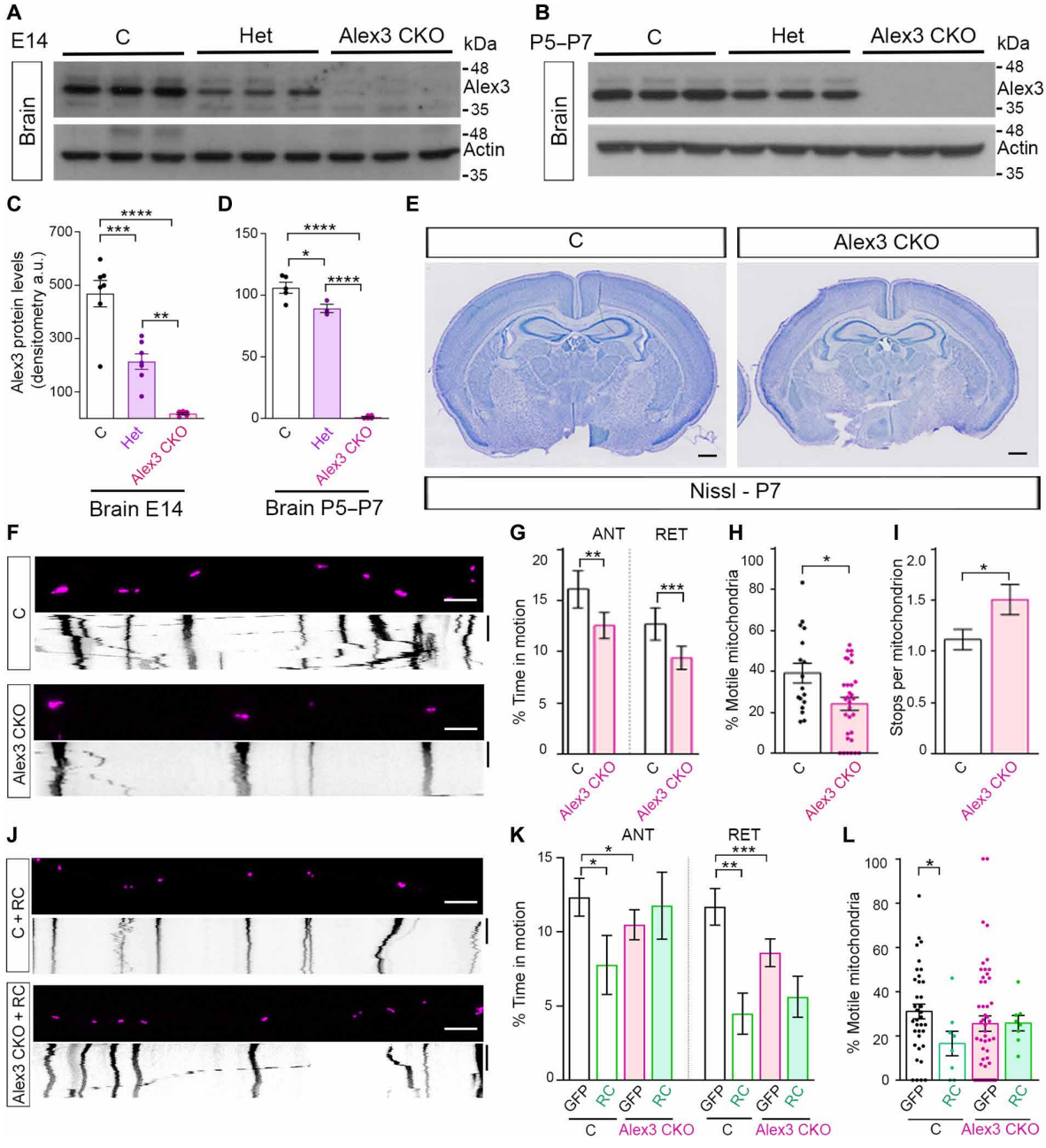

Fig. 4. Characterization of the *Armcx3*$^{fl/fl}$/*Nestin-Cre* mouse line. (**A** and **B**) Representative Western blots from brain lysates of Alex3 and actin from *Armcx3*$^{fl/fl}$ control (C), Het, and Alex3 CKO mice at E14 (A) and P5 to P7 (B). (**C** and **D**) Western blot quantification at E14 (C) and P5 to P7 (D). $n = 3$ to 7 embryos (C) and 3 to 5 mice per genotype analyzed in three independent experiments. (**E**) Representative images of brain slices from control and Alex3 CKO mice stained with Nissl. (**F**) Images and kymographs from axons of control or Alex3 CKO mice neurons expressing mitoDsRed. (**G** to **I**) Graphical representation of the percentage of time in motion (G), percentage of motile mitochondria (H), and number of stops per mitochondrion (I). $n = 264$ (control) and 498 (Alex3 CKO) mitochondria from 17 (C) and 32 (Alex3 CKO) independent axons from $n = 3$ to 5 mouse embryos per condition analyzed in three independent experiments. (**J**) Images and kymographs from control or Alex3 CKO mice axons expressing GFP and mitoDsRed in the presence of $G\alpha_q$R183C (RC). (**K** and **L**) Bar graphs showing the percentage of time in motion (K) or percentage of motile mitochondria (L) in Alex3 CKO axons expressing $G\alpha_q$R183C. $n = 431$ (control), 133 (control RC), 685 (Alex3 CKO), and 154 (Alex3 CKO RC) mitochondria from 36 (control), 8 (control RC), 52 (Alex3 CKO), and 8 (Alex3 CKO RC) independent axons from $n = 3$ to 5 mouse embryos per condition analyzed in five independent experiments. Scale bars, 500 μm (E) and 5 μm (F) and (J). Time bars, 300 s. Data are means ± SEM. Statistical analyses: One-way ANOVA with Bonferroni post hoc test for (C) and (D), Mann-Whitney *U* test for (G) to (I), and Kruskal-Wallis with Dunn's multiple comparison test for (K) and (L). *$P < 0.05$, **$P < 0.01$, ***$P < 0.001$, and ****$P < 0.0001$.

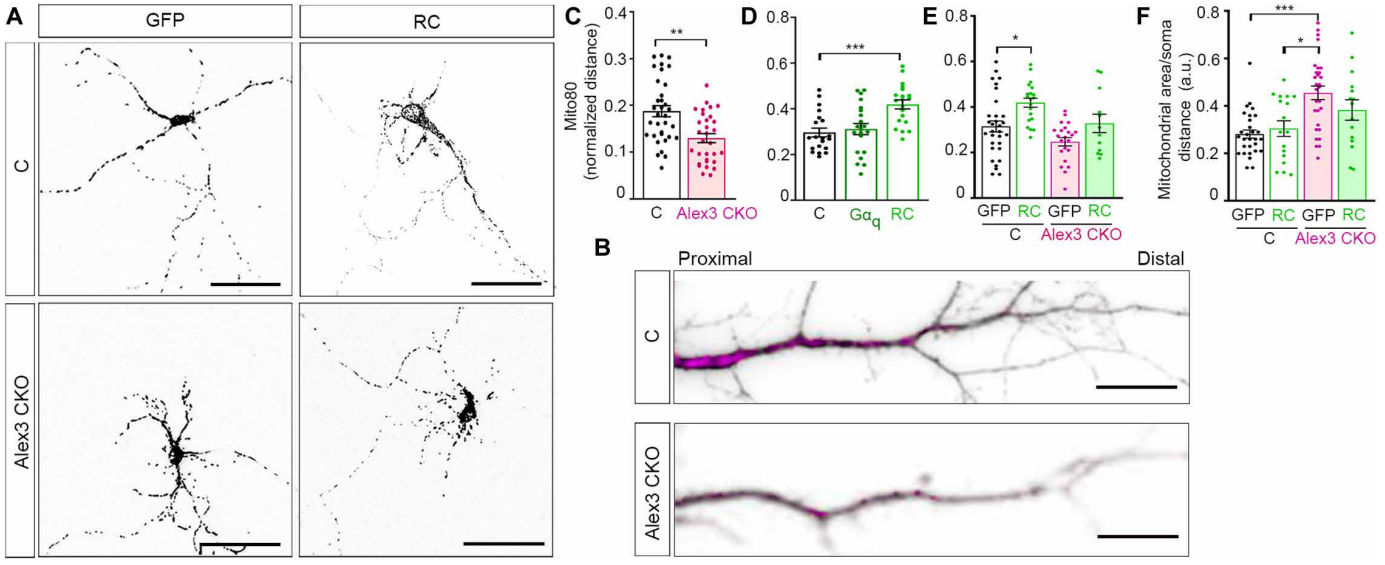

Fig. 5. Mitochondrial distribution in dendrites depends on Alex3 and Gα$_q$. (**A**) Mitochondrial distribution in control (C) or Alex3 CKO neurons at 7 DIV expressing GFP and mitoDsRed (GFP) in the presence or absence of Gα$_q$R183C (RC). (**B**) Dendritic processes (gray) showing mitochondrial distribution (magenta) in control and Alex3 CKO dendrites. (**C**) Length-normalized Mito80 values from control or Alex3 CKO neurons at 14 DIV. $n = 34$ (control) and 31 (Alex3 CKO) neurons from $n = 3$ to 5 mouse embryos per condition analyzed in three independent experiments. (**D**) Length-normalized Mito80 values from control neurons at 6 to 7 DIV expressing mitoDsRed and GFP without (GFP) or with WT Gα$_q$ (Gα$_q$) or Gα$_q$R183C (RC) expression. $n = 23$ (GFP), 21 (Gα$_q$), and 13 (RC) neurons from $n = 8$ to 12 mouse embryos per condition analyzed in four independent experiments. (**E**) Length-normalized Mito80 values from control and Alex3 CKO neurons at 6 to 7 DIV expressing mitoDsRed without (GFP) or with Gα$_q$R183C (RC) expression. $n = 54$ (control GFP), 20 (control RC), 22 (Alex3 CKO GFP), and 12 (Alex3 CKO RC) neurons from $n = 3$ to 5 mouse embryos per condition analyzed in five independent experiments. (**F**) Mitochondrial area in the soma of control or Alex3 CKO neurons with (GFP) or without Gα$_q$R183C (RC) expression. $n = 29$ (control GFP), 17 (control RC), 29 (Alex3 CKO GFP), and 15 (Alex3 CKO RC) somas from $n = 3$ to 5 mouse embryos per condition analyzed in five independent experiments. Scale bars, 50 μm (A) and 20 μm (B). Data are presented as means ± SEM. Statistical analyses: Unpaired two-tailed Student's *t* test with Welch correction for (C), two-way ANOVA with Bonferroni post hoc test for (D) and (E), and Kruskal-Wallis with Dunn's multiple comparison test for (F). $^*P < 0.05$, $^{**}P < 0.01$, and $^{***}P < 0.001$.

NT in either control or Alex3 CKO neurons (Fig. 6, H and I) resulted in dendritic phenotypes largely similar to control neurons (Fig. 6, B and C), whereas the expression of the Gα$_q$ mutant that cannot bind to PLCβ (RCAA) (Fig. 6, H and I) resulted in dendritic phenotypes similar to those of Gα$_q$ R183C-expressing neurons (Fig. 6, D and E). These results suggest that the effects of Gα$_q$ Alex3 on dendritic growth are independent of the PLCβ pathway. Last, we found that knocking down Gα$_q$ resulted in decreased dendritic length and altered dendritic patterns (fig. S7, A and B), which were not observed when Gα$_q$ was knocked down (Gα$_q$ KD) in Alex3 CKO neurons (fig. S7, A and C). These results indicate that the dendritic effects caused by the inactivation of *Armcx3* can be partially overcome by the active form of Gα$_q$ and, conversely, that Alex3 is required for most of the dendritic phenotypes driven by expression of active Gα$_q$.

Lack of Alex3 leads to altered expression of endoplasmic reticulum stress response and OXPHOS respiratory complexes

Overall, the absence of Alex3 produced defects in mitochondria motility and distribution in neurites that resulted in altered dendrite arborization in a mechanism dependent on Gα$_q$ activity. To evaluate the impact of Alex3 depletion on mitochondrial homeostasis, we analyzed the expression levels of mitochondrial respiratory proteins. Western blotting analysis detected a decrease in the levels of mitochondrial respiratory complexes, suggesting altered OXPHOS expression in Alex3 CKO mice (fig. S8, A and B), consistent with those observed in *Miro1/2* null mutants and in Gα$_q$ and Gα KO cells (*24*, *42*).

Next, we analyzed the contribution of endoplasmic reticulum (ER) stress response proteins. The levels of C/EBP homologous protein (CHOP) were reduced in Alex3 CKO brains, whereas phosphorylation of inositol-requiring enzyme 1 (IRE1) and eukaryotic translation initiation factor 2 alpha (eiF2α) abundance was unaltered (fig. S8, C to L). Binding immunoglobulin protein (BIP) and B-cell lymphoma 2 (Bcl-2) protein levels were similar between control and Alex3 CKO mice (fig. S8, M to P). These findings suggest alterations in the expression of the machinery that regulates mitochondrial respiration and ER stress response upon *Armcx3* deletion.

CNS-specific inactivation of *Armcx3* leads to motor deficits and neuronal death

Alex3 CKO mice were smaller than littermate controls, exhibited severe motor alterations (lack of balance, tremors, and impaired locomotion and coordination) (fig. S9, A and B), and usually died around P7 to P9. Mice with constitutive or neuron-specific deficiency in Gα$_q$ are also smaller than control littermates (*25*, *46*). Alex3 CKO mice had slightly smaller brains than littermate controls, which was also noticeable in histological sections (Fig. 4E and fig. S9, C and D). Despite this reduction, the overall brain anatomy and organization, including layer distribution in structures such as the cerebral cortex and cerebellum, were similar in Alex3 CKO and control mice (fig. S9, C to K). Staining the cerebellum of Alex3 CKO

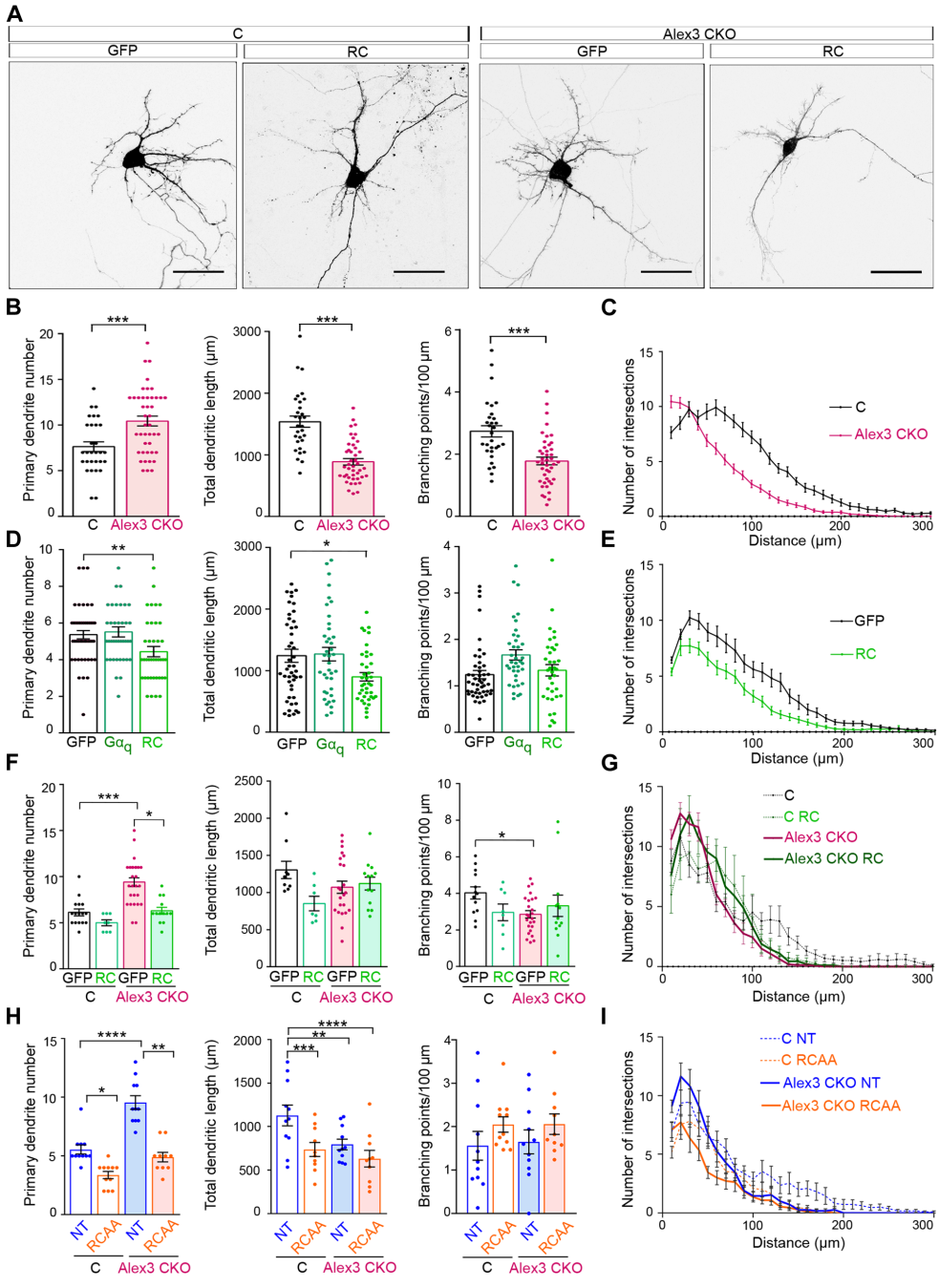

Fig. 6. Alex3 and Gα$_q$ regulate dendritic arborization. (**A**) Control (C) and Alex3 CKO neurons at 7 DIV expressing GFP and mitoDsRed without (GFP) or with Gα$_q$R183C (RC) expression. (**B** and **C**) Control and Alex3 CKO neurons at 14 DIV expressing GFP were analyzed for number of primary dendrites, total length of dendritic tree, and number of branching points. (**C**) Sholl analysis of branching points. For (B) and (C), $n = 30$ (control) and 42 (Alex3 CKO) neurons from $n = 3$ to 5 mouse embryos per condition analyzed in five independent experiments. (**D** and **E**) Neurons at 7 DIV expressing mitoDsRed and GFP without (GFP) or with WT Gα$_q$ (Gα$_q$) or Gα$_q$R183C (RC) expression, analyzed as in (B) and (C). For (D) and (E), $n = 47$ (GFP), 39 (Gα$_q$), and 39 (RC) neurons from $n = 8$ to 12 mouse embryos per condition analyzed in four independent experiments. (**F** and **G**) Control or Alex3 CKO neurons at 7 DIV expressing mitoDsRed and GFP without (GFP) or with Gα$_q$R183C (RC) were analyzed as in (B) and (C). $n = 16$ (control GFP), 8 (control RC), 27 (Alex3 CKO GFP), and 13 (Alex3 CKO RC) neurons for number of primary dendrites; $n = 9$ (control GFP), 7 (C RC), 23 (Alex3 CKO GFP), and 13 (Alex3 CKO RC) neurons for total length of dendritic tree; and $n = 13$ (control GFP), 8 (control RC), 25 (Alex3 CKO GFP), and 13 (Alex3 CKO RC) neurons for number of branch points. (**G**) Sholl analysis of branching points in the neurons described in (F). For (G), $n = 32$ (control GFP), 39 (control RC), 9 (Alex3 CKO GFP), and 43 (Alex3 CKO RC) neurons. For (F) and (G), neurons were from $n = 8$ to 12 mouse embryos per condition analyzed in four independent experiments. (**H** and **I**) Control or Alex3 CKO neurons expressing mitoDsRed and GFP-Gα$_q$NT (NT) or GFP-Gα$_q$R183C/R256A/T257A (RCAA) analyzed as in (B) and (C). For (H) and (I), $n = 10$ (control RCAA and Alex3 CKO RCAA) or 11 (control NT and Alex3 CKO NT) neurons each from $n = 3$ mouse embryos per condition analyzed in three independent experiments. Scale bars, 50 μm (A). Data are means ± SEM. Statistical analyses: Unpaired two-tailed Student's *t* test with Welch correction for (B) and Kruskal-Wallis with Dunn's multiple comparison test for (D), (F), and (H). $^*P < 0.05$, $^{**}P < 0.01$, $^{***}P < 0.001$, and $^{****}P < 0.0001$.

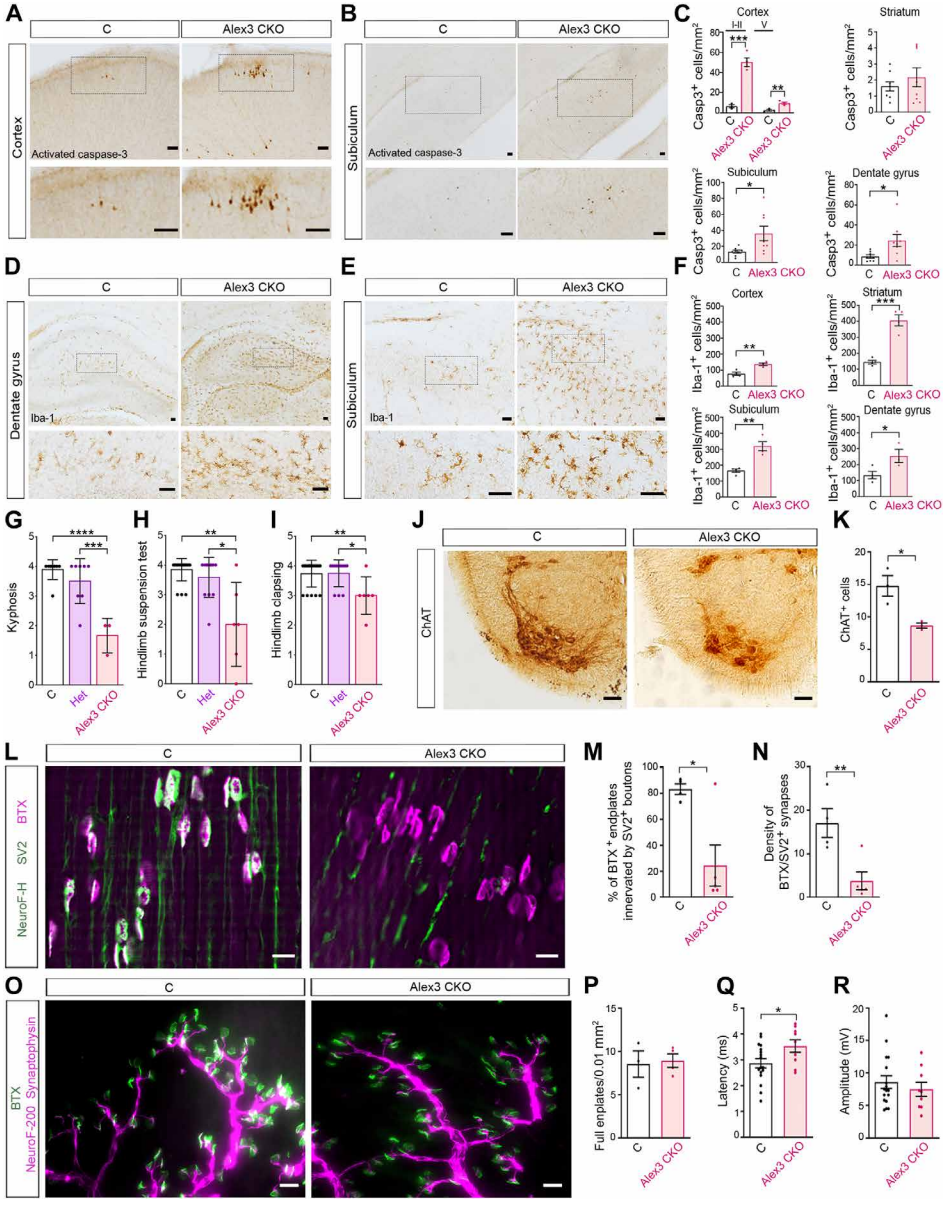

Fig. 7. In vivo Alex3 deficiency increases cell death and microgliosis and leads to neuromuscular synaptic and electrophysiological deficits. (**A** and **B**) Representative photomicrographs of activated caspase-3 in the cortex (A) and subiculum (B). (**C**) Quantification of the density of activated caspase-3–positive cells in layers I, II, and V of the cortex ($n = 3$ or 4 mice per genotype), striatum ($n = 8$ mice per genotype), subiculum ($n = 8$ mice per genotype), and dentate gyrus ($n = 8$ mice per genotype) analyzed in two independent experiments. (**D** and **E**) Representative photomicrographs of Iba-1–positive cells in the dentate gyrus (D) and subiculum (E). (**F**) Quantification of microglial cell density in the cortex, the striatum, the subiculum, and the dentate gyrus. $n = 3$ or 4 mice per genotype analyzed in two independent experiments. (**G** to **I**) Motor behavior of control (C), heterozygous (Het), and Alex3 CKO mice at P5 to P7 analyzed in three or four independent experiments. For kyphosis (G), $n = 3$ to 9 mice per genotype. For hind limb suspension test (H), $n = 6$ to 19 mice per genotype. For clasping test (I), $n = 6$ to 19 mice per genotype. (**J** and **K**) Choline acetyltransferase (ChAT)–positive motor neurons in the thoracic ventral horn of the spinal cord in motor neurons in control and Alex3 CKO and mice. $n = 3$ mice per genotype analyzed in two independent experiments. (**L**) Representative images of the neuromuscular junctions of the diaphragm muscle stained for rhodamine-conjugated bungarotoxin (BTX; magenta; postsynaptic acetylcholine receptors at endplates), neurofilament SMI-312, and SV2 (green; axons and presynaptic terminals, respectively). (**M** and **N**) Quantification of the percentage of BTX-positive endplates innervated by SV2-positive boutons (M) and the density of synapses double labeled with BTX and SV2 (N) in control and Alex3 CKO mice. $n = 4$ or 5 mice per genotype analyzed in two independent experiments. (**O**) Representative images of the neuromuscular junctions of the gastrocnemius muscle stained for Alexa Fluor 488 bungarotoxin (green), neurofilament 200, and synaptophysin (magenta). (**P**) Density of double-labeled synapses (full endplates) in the gastrocnemius muscle. $n = 3$ or 4 mice per genotype analyzed in two independent experiments. (**Q** and **R**) In vivo motor nerve conduction analysis of peripheral nerve latency, done by stimulating at the sciatic nerve and recording at the gastrocnemius muscle (Q) and amplitude (R). $n = 9$ to 17 mice per genotype analyzed in four independent experiments. Scale bars, 50 μm (A, B, D, E, and J), 10 μm (L), and 20 μm (O). Data are means ± SEM. Statistical analyses: Unpaired two-tailed Student's *t* test for (C; cortex and striatum), (F), (K), (M), (P), (Q), and (R); unpaired two-tailed Student's *t* test with Welch's correction for (C; subiculum and dentate gyrus) and (N); one-way ANOVA with Bonferroni post hoc test for (G) and (I); and Kruskal-Wallis with Dunn's multiple comparison test for (H). $^*P < 0.05$, $^{**}P < 0.01$, $^{***}P < 0.001$, and $^{****}P < 0.0001$.

mice for calbindin revealed reduced density, cell body size, and dendritic tree width of Purkinje cells (fig. S9, L to O).

Considering the defects on dendritic density, OXPHOS and ER stress response proteins levels, and the smaller brain size of Alex3 CKO mice, we investigated whether *Armcx3* deficiency affects neuronal cell death. We quantified apoptotic cells that were positive for cleaved caspase-3 in several brain regions. There was an increase in the number of apoptotic cells in Alex3 CKO mice, which was statistically significant in layers II to III of the cerebral cortex, the subiculum, the striatum, and the dentate gyrus (Fig. 7, A to C). In addition, using the microglial marker ionized calcium binding adaptor molecule 1 (Iba1), we detected a widespread increase in microgliosis in the absence of Alex3 across all regions studied (Fig. 7, D to F). We conclude that deficiency of Alex3 in vivo results in increased neuronal death and neuroinflammation.

Deletion of *Armcx3* results in decreased number of motor neurons and in physiological alterations

We next performed motor behavior–related tests. Alex3 CKO mice presented with persistent kyphosis, which might indicate loss of muscle tone, and exhibited deficits in the hind limb suspension and the hind limb clasping tests, which suggests decreased muscle strength (Fig. 7, G to I). We then determined whether spinal cord motor neurons were affected by analyzing choline acetyltransferase (ChAT) expression. We found fewer ChAT-positive motor neurons in the ventral horn of the thoracic spinal cord of Alex3 CKO mice compared with littermate controls (Fig. 7, J and K). To investigate whether neuromuscular synapses were altered, the neuromuscular junctions (NMJs) of diaphragm muscles were visualized by labeling postsynaptic acetylcholine receptors at endplates with α-bungarotoxin and axons and presynaptic terminals with synaptobrevin 2 (SV2). There was a decrease in the density of SV2-labeled endplates in Alex3 CKO mice compared with controls, suggesting impairment in these neuromuscular synapses in the absence of Alex3 (Fig. 7, L to N). In contrast, the density of NMJs in hindlimb gastrocnemius muscles was similar in Alex3 CKO and control mice (Fig. 7, O and P). Last, motor nerve conduction tests were performed at P5 to investigate the physiological consequences of *Armcx3* inactivation. After sciatic nerve stimulation, we found increased latencies of compound muscle action potentials (CMAPs) in the gastrocnemius muscle of Alex3 CKO mice. In contrast, the amplitude of CMAPs did not differ between genotypes (Fig. 7, Q and R). These results suggest muscle-specific NMJ alterations in Alex3 CKO mice. Moreover, alterations in the *ARMCX3* gene have been reported in several neurological disorders (table S1). Together, our data demonstrate that loss of Alex3 in CNS produces alterations in dendritic morphology and increased neural apoptosis, motor neuron loss, and inflammation, causing severe motor alterations (Fig. 8).

DISCUSSION

The present study provides evidence for a role for Alex3 as a component of the $G\alpha_q$ signaling pathway that regulates mitochondrial trafficking and dynamics in neurons through its link to the Miro/Trak trafficking complex (*4*, *6*, *14*, *47*–*50*). $G\alpha_q$ and Alex3 interacted functionally in the regulation of neuronal mitochondria distribution and transport as well as in dendritic growth and complexity. Because $G\alpha_q$ signals downstream of multiple important GPCRs (metabotropic glutamate receptors, muscarinic receptors, and many neuropeptide receptors), our findings suggest a molecular pathway by which various extracellular signals may control mitochondrial dynamics and functions.

The mitoproteome analysis identified Alex3 as a binding partner of $G\alpha_q$. We focused on this protein because it is a component of the mitochondria motility complex (*14*) and it contains armadillo domains that interact with Gα subunits (*44*, *51*–*53*) and GPCRs (*12*). Moreover, Alex3 belongs to the Eutherian-specific family of mitochondrial proteins present in the nervous system. We provide evidence that Alex3 directly bound through its armadillo domain to $G\alpha_q$, predominantly its nonconstitutively active form ($G\alpha_q$ or $G\alpha_q$R183C but not $G\alpha_q$Q209L). We also showed that constitutively active $G\alpha_q$ partly reverted the phenotype of mitochondrial aggregation near cell bodies and the neuronal arborization defects observed upon *Armcx3* deletion, suggesting a functional interaction between both proteins. Taking into account this and the effects of other armadillo domain–containing proteins, we suggest that Alex3 may potentiate the role of GPCRs to control mitochondrial movement (*19*, *54*) by acting as an adaptor, scaffolding, or modulator (*44*, *55*). In contrast, depletion of $G\alpha_q$ diminished Alex3 abundance. Phosphorylation of Alex3 through the canonical PLCβ-PKC axis by Wnt protects from protein degradation (*38*), suggesting a regulatory feedback loop in which $G\alpha_q$ activation of the canonical pathway controls Alex3 abundance. Overall, this additional regulatory level could contribute to the arrest of mitochondrial movement in response to changes of directionality upon GPCR stimulation.

Other GPRASP/ARMCX family members may interact with G proteins, particularly considering that Armc10 and Alex1 also associate with Miro1 and share some physiological functions with Alex3 (*16*, *17*) and that Armc10 was found in $G\alpha_q$ immunoprecipitates (fig. S3A). Moreover, GPRASP1 interacts with the δ opioid receptor and with the heterotrimeric Gαs subunit (*51*), and Armc10 is phosphorylated by the GPCR effector adenosine 5′-monophosphate kinase (AMPK) (*56*). Alex3 also interacts with guanine nucleotide binding protein subunit alpha S (GNAS) and guanine nucleotide binding protein subunit alpha T2 (GNAT2) (Gαs and Gαt proteins) (*57*, *58*). Thus, we propose that members of the GPRASP/ARMCX family may modulate GPCR signaling by interacting with either GPCRs (GPRASP subfamily) or Gα subunits (ARMCX subfamily).

Our data provide evidence that mitochondrial transport is regulated by the direct binding of $G\alpha_q$ and Alex3 to the trafficking machinery. Endogenous Alex3 interacts with Miro1 and Trak2, and $G\alpha_q$ association with Alex3 and Miro1 promoted kinesin-mediated anterograde transport, likely by reducing the interaction between Trak2 and dynein. When $G\alpha_q$ is fully activated by GPCRs or other GEFs (which is mimicked by expressing the $G\alpha_q$Q209L mutant form or overexpressing $G\alpha_q$R183C), Alex3 and GTP-bound $G\alpha_q$ dissociate from Miro1 and the adaptor proteins. This resulted in the detachment of the Miro1/Trak complex from microtubules and diminished mitochondrial transport or arrest (Fig. 3M and 8A) (*4*, *14*, *41*). In addition, the absence of Alex3 led to multiple mitochondrial phenotypes, including decreased transport and accumulation in cell bodies, concomitant to aberrant dendritic trees. The activation of the $G\alpha_q$ pathway in Alex3 CKO neurons partially reverted these phenotypes (Fig. 8B), further supporting a physiological link between $G\alpha_q$/Alex3 and mitochondrial trafficking. Alex3 deficiency leads to transport alterations similar to, although less marked than, those observed after Alex3 complex disassembly upon $G\alpha_q$ activation and Ca^{2+} rise (Fig. 8, A and B) (*4*, *14*, *41*). In conclusion, our data support that G protein signaling at mitochondria regulates dynamics through specific $G\alpha_q$/Alex3 interactions, in addition to canonical Ca^{2+}-dependent signaling pathways (*6*, *54*, *59*–*63*). Further

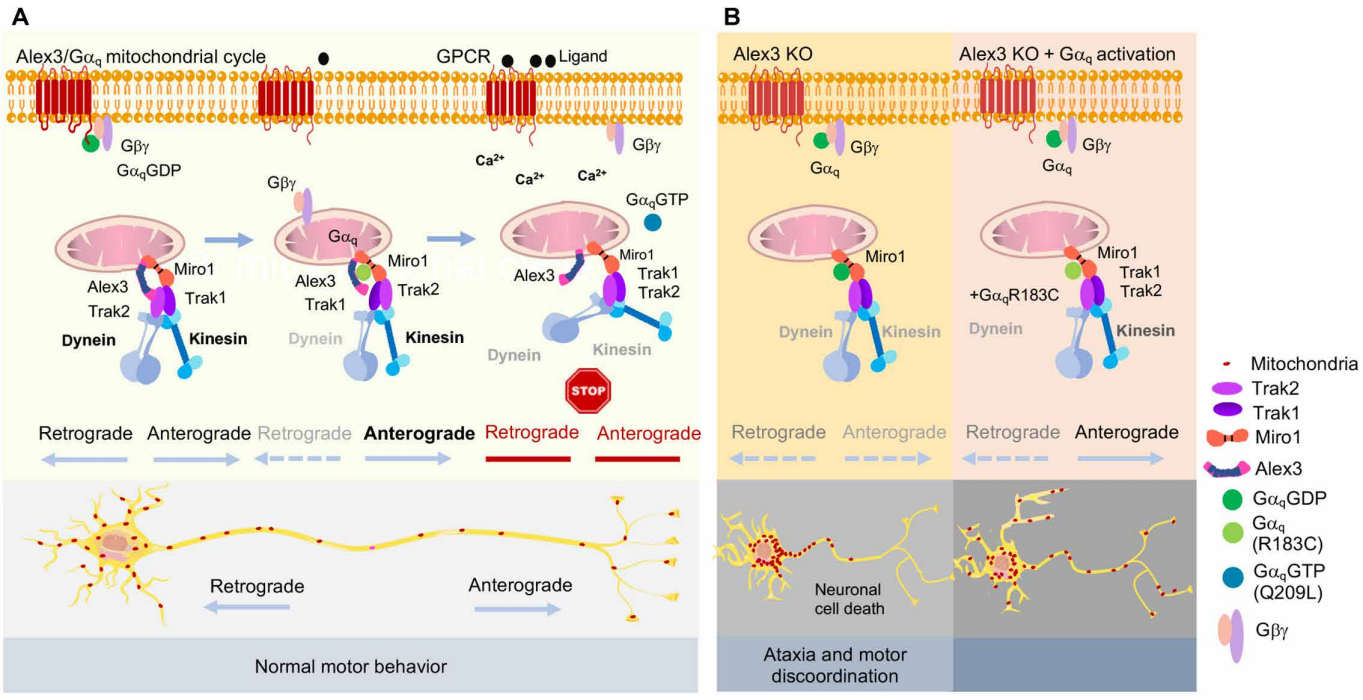

Fig. 8. Molecular model of Gα$_q$ signaling in the presence and absence of Alex3. (**A**) Under normal physiological conditions, Alex3 interacts with Miro1 and Trak2, and the association of Gα$_q$ with Alex3 and Miro1 favors anterograde transport, diminishes the Trak2 and dynein interaction, and supports kinesin transport. Further activation of Gα$_q$ by GEFs (either GPCRs or other GEFs), a state similar to expression of the Q209L mutant or to high Gα$_q$R183C expression, produces the dissociation of Alex3 and of Gα$_q$ from Miro1 and the Trak proteins, and the remaining complex detaches from microtubules, resulting in arrested movement, a process facilitated by increased Ca^{2+} levels. This physiologic cycle allows the distribution of mitochondria along neuronal dendrites and axons through anterograde and retrograde movements (bottom). (**B**) In the absence of Alex3, anterograde and retrograde movements of mitochondria are decreased, and neurons present with altered dendritic arborization and accumulation of mitochondria around the soma, resulting in increased neuronal cell death and motor impairments (bottom). The presence of the constitutively active Gα$_q$R183C partially reverses deficits in mitochondrial movement, dendritic arborization, and mitochondrial accumulation around the soma associated with Alex3 deficiency.

studies are needed to clarify the molecular changes caused by the lack of Alex3 on both Gα$_q$ signaling and transport mechanisms.

Mitochondrial cannabinoid receptor 1 (CB1) receptors mediate distinct mitochondrial processes, synaptic transmission, and memory functions (*21*, *23*, *56*). Other mitochondrial GPCRs, including angiotensin II receptor type-1 (AT1R) (*64*), purinergic receptor P2Y1 (P2Y1R) and purinergic receptor P2Y2 (P2Y2R) (*59*), 5-hydroxytryptamine (serotonin) receptor 4 (5HT4R) (*61*), and melatonin membrane receptor 1 (MT1R) (*62*), affect respiration, Ca^{2+} buffering or neuronal cell death. The intracellular mitochondrial role of Gα$_q$ mediated by Alex3 interaction and Miro1 suggests that some physiological processes previously thought to be mediated by plasma membrane receptors may be due to the local action of GPCRs at mitochondria.

Altered dendritic development correlates with defects in mitochondrial localization or trafficking machinery (*45*, *65*, *66*). The present study highlights the relevance of Alex3 and Gα$_q$ in distinct neural processes (dendritic formation, synaptogenesis, and neuronal survival), which are likely involved in the occurrence of motor deficits. Moreover, Gα$_q$ null mutant mice also present with motor dysfunction (*27*), and *Miro1* ablation results in reduced dendrites without locomotion defects (*45*), which may be due to *Miro1* ablation occurring postnatally.

Our findings show that loss of *Armcx3* results in a reduction of NMJs in the diaphragm but not in the hindlimb gastrocnemius muscle, correlating with the absence of effects on synaptic CMAPs. These results could be related either to differential motoneuron vulnerability or to compensatory nerve sprouting, as has been described during development, in partially denervated muscles and in neuromuscular diseases (*67*, *68*). Alternatively, delayed nerve growth (as seen in Alex3 CKO hippocampal dendrites) might account for these differences, considering the longer distance between the brain stem and the diaphragm compared with that of the spinal cord and the hindlimb gastrocnemius muscle.

Loss-of-function *ARMCX3* mutations have not been detected, and a very low number of missense variants in *ARMCX3* have been identified in hemizygosis in human populations (table S1), suggesting that this gene may be intolerant of loss-of-function mutations. Furthermore, large duplications affecting *ARMCX3* are associated with schizophrenia and autistic disorders (*69*), whereas *ARMCX3* variants are associated with metabolic diseases (*70*) and *ARMCX3* is the most prominent gene linked to sleep-disordered breathing hypoxia (*71*) (table S1). *GNAQ* (which encodes Gα$_q$) mutations lead to motor and cognitive dysfunctions (*25*–*27*) and cause seizures and mental retardation (*72*–*74*), whereas mutations and variants in the functionally related genes *TRAK2* and *RHOT1/2* (which encodes Miro1/2) are associated with autism disorders and late-onset neurodegenerative diseases (*75*–*87*) (table S1). Miro1 decreases mitophagy through parkin, which is encoded by a Parkinson's disease–associated gene (*38*, *63*).

Mitochondrial dysfunction and loss of dendritic and axonal complexity are hallmarks of many neurodegenerative disorders, including

ataxic disorders (*88*–*90*) and late-onset neurodegenerative diseases such as Alzheimer's disease (*7*–*10*). Armc10 prevents amyloid-β–induced mitochondrial fission and neuronal death (*16*). The present study shows that the Alex3/Gα_q complex is necessary for correct dendritic arborization and mitochondrial distribution in neurons. Moreover, the lack of Alex3 in vivo results in altered expression of mitochondrial respiratory complexes and ER stress response elements. Alex3 CKO mice display increased neuronal death in many CNS regions, including the spinal cord, in association with decreased peripheral synaptic innervation and severe motor deficits, which also occur in mitochondrial diseases (*67*). Given the molecular and functional interactions between Alex3 and Gα_q and their coordinated actions on mitochondrial dynamics and dendritic growth, the phenotypes caused by *Armcx3* inactivation are likely linked to the lack of a functional Alex3/Gα_q interaction (Fig. 8). Together, our findings lead us to propose a model in which disruption of the Alex3/Gα_q complex results in aberrant mitochondrial trafficking and distribution, altered ER stress and respiratory protein levels, decreased neurite growth, and, lastly, neuronal cell death. It remains to be determined how extracellular signals regulate these processes through GPCR-mediated activation of Gα_q-dependent pathways and, considering the above genetic data, the likely contribution of the Eutherian-specific Alex3/Gα_q complex in the pathogenesis of human neurodegenerative and psychiatric disorders linked to mitochondrial dysfunction.

MATERIALS AND METHODS

Plasmid vectors

pcDNA3.1(+) was from Invitrogen, and pEGFP was from BD Biosciences. Mitochondrial-targeted DsRed and GFP (pmitoDsRed and pmitoGFP) and pcDNA3-KIF5c-Myc were a gift from A. Zorzano (IRB Barcelona, Spain) (*91*). pCDH-Miro1-Cherry, pCDH-Miro1-GFP, and pCDH-Tom20-Cherry plasmids were a gift from M. Johnson (MRC Mitochondrial Biology Unit, UK). Alex3 expression vectors [pSecTag-Myc-Alex3, pEGFP-Alex3, pEGFP-Alex3-NT, pEGFP-Alex3-CT, pEGFP-Alex3-ΔCt (DCT), pEGFP-Alex3-ΔNt (DCN), pEGFP-Alex3 (1 to 104), and pEGFP-Alex3 (1 to 44)] were previously described (*14*). GST-Alex3 constructs were generated and subcloned into pGEX2T and pGEX4T vectors (Pharmacia) with the following oligonucleotides: GST-Alex3-FL (30 to 379) and GST-Alex3-NT (30 to 111), 5′-CGCGG ATCCGGAAGAAAGCAGAACAAGGAG-3′ (forward); GST-Alex3-FL (30 to 379), GST-Alex3-CT (111 to 379), and GST-Alex3-CT2 (273 to 379), 5′-GCGGAATTCCTTCCTGACTCTTTGGGAACAT C-3′ (reverse); GST-Alex3-NT (30 to 111), 5′-GCGGAATTCCAGG AGAAGCCCTTTTCTGTAC-3′ (reverse); GST-Alex3-CT (111 to 379) and GST-Alex3-CT1 (111 to 279), 5′-CGCGGATCCCCTAAT TCAGACGATACTGTTTTGTC-3′ (forward); GST-Alex3-CT1 (111 to 272), 5′-CCGCTCGAGCTTTCAGCCAGATTCAAAAGGAGC-3′ (reverse); GST-Alex3-CT2 (273 to 379), 5′-CGCGGATCCAATCCAG CCATGACTAGAGAACTGC-3′ (forward).

pcDNA3-Gα_q, pcDNA3-Gα_qR183C, and pcDNA3-Gα_qQ209L were cloned from pCIS vectors from M. I. Simon (Caltech) (*92*) and have been previously described (*93*). The constitutively active Gα_q mutant that lacks the ability to interact with PLCβ (QLAA) was provided by R. Lin (Stony Brook University, NY, USA). pcDNA-Gα_qR183C/R256A/T257A was provided by F. Mayor (CBM, Spain). pCNA-Myc-GRK2 was a gift from J. L. Benovic (the Kimmel Cancer Center, USA). pcDNA1-GFP-Gα_qR183C and pcDNA1-Gα_qNT-GFP (amino acids 1 to 124) were generously provided by C. Berlot (Yale University School of Medicine, USA) (*24*). pcDNA3.1-Gβ-FLAG and pcDNA3.1–Gγ1–hemagglutinin (HA) were from the Missouri S&T cDNA Resource Center (www.cdna.org/home.php). pLKO1-shGq (Gα_q KD 1) sequence was obtained from MISSION Sigma (Functional Genomics Core Facility, IRB Barcelona) as previously described (*24*) and subcloned into pLKO.3G vector to obtain pLKO.3G-shGq (Gα_q KD 2). pLKO.3G-shscr (SCR) was from MilliporeSigma. pRK5-Myc-Miro1, pGW1-TRAK1-HA, pGW1-TRAK2-HA, pEGFP-synaptophysin and pCAGIRES-mitoDsRed were provided by J. Kittler (University College of London, UK). To generate pIRES-mitoDsRed-Gα_q, pcDNA3-Gα_q was subcloned into pCAGIRES-mitoDsRed vector using the primers 5′-CCGGGCTAGCATGACTCTGGAGTCCAT CATGGCG-3′ and 5′-GGCCCGATCGTTAGACCAGATTGTACTC CTTCAGGTTC-3′. pIRES-mitoDsRed-Gα_qR183C was generated by introducing a point mutation in pIRES-mitoDsRed-Gα_q using the QuikChange II Site-Directed Mutagenesis Kit (Agilent) and the primers 5′-GACGTGCTTAGAGTTTGTGTCCCCACTACAGGGA-3′ and 5′-TCCCTGTAGTGGGGACACAAACTCTAAGCACGTC-3′. pcDNA3-Gα_qR183C/R256A/T257A and pcDNA1-GFP-Gα_qR183C/R256A/T257A were generated by introducing point mutations in two different reactions from pcDNA3-Gα_qR183C and pcDNA3-GFP-Gα_qR183C, respectively, using the QuikChange II Site-Directed Mutagenesis Kit (Agilent) and the following primers: polymerase chain reaction 1 (PCR1), 5′-GAGCAAAGCACTCTTTGCAACAATTATCA CCTACC-3′ (forward) and 5′-GGGGTAGGTGATAATTGTTGCAAA GACTGCTTTGCT-3′ (reverse); PCR2, 5′-GCAAAGCACTCTTTGC AGCAATTATCACCTACCCC-3′ (forward) and 5′-GGGGTCGGTGA TAATTGCTGCAAAGAGTGCTTTGC-3′ (reverse). pAAV–hSyn–hM3D (Gα_q)–mCherry was a gift from B. Roth (Addgene plasmid #50474).

Antibodies and reagents

Primary antibodies and reagents were as follows: Alex3 (25705-1-AP, ProteinTech; 1:1000) (the antibody recognizes a major band at 43 kDa and two specific secondary bands of lower molecular weight and was validated using MEFs deficient in Alex3), β-tubulin [MMS-431P, Covance (1:10,000) and T2200, Merck-Sigma (1:10,000)], GFP [A11122, Invitrogen (1 : 1000) and gta-20, ChromoTek (1:200)], DsRed (632496, Clontech; 1:2000), GST (SAB4200237, Merck-Sigma; 1 : 2000), Myc [05-724, Millipore (1 : 2000) and M4439, Merck-Sigma (Western blot, 1:2000; immunofluorescence, 1:200); yta-20, ChromoTek (1:200)], HA [11867423001, Roche (1:2000) and A2095, Merck-Sigma (1:25)], FLAG (F1804-50UG, Merck-Sigma; 1:1000), Gα_q [G7, sc-136181, Santa Cruz Biotechnology (1 : 1000); E17, sc-393, Santa Cruz Biotechnology (1 : 1000); C19, sc-392, Santa Cruz Biotechnology (1 : 1000); and 612704, BD Biosciences (1 : 1000)] (antibodies were validated using MEFs deficient in Gα_q and Gα), Miro1 (HPA010687, Merck-Sigma; 1 : 1000), glyceraldehyde-3-phosphate dehydrogenase (GAPDH) (14C10, Cell Signaling Technology; 1 : 1000), heat shock protein 90 (HSP90) (610418, BD Biosciences; 1 : 2000), Tom 20 [sc-17764, Santa Cruz Biotechnology (1:1000) and sc-11415, Santa Cruz Biotechnology (1:1000)], dynein (sc-13524, Santa Cruz Biotechnology; 1:1000), OXPHOS complex IV subunit 1 (459600/C0941, Life Technologies), pIRE (pSer^{724}) (NB-100-2323, Novus; 1:0000), Bcl2 (50E3) (2870, Cell Signaling Technology; 1:1000), BIP (3183, Cell Signaling Technology; 1:1000), CHOP (L63F7) (2895, Cell Signaling Technology; 1:1000), eIF2α (9722, Cell Signaling Technology; 1:1000), peIF2α (Ser^{51}) (9721, Cell Signaling Technology; 1:1000), IRE1α (14C10) (3294, Cell Signaling Technology; 1:1000), OXPHOS (110413, Abcam; 1:1000),

Iba-1 (019-19741, Wako; 1:1000), cleaved caspase-3 (9664S, Cell Signaling Technology; 1:1000), ChAT (AB144P, Merck-Sigma; 1:100), cut like homeobox 1 (Cux1) (SC-13024, Santa Cruz Biotechnology; 1:250), (COUP-TF)–interacting protein 2 (CTIP2) (ab18465, Abcam; 1:500), calbindin (300, Swant; 1:5000), SV2A [SV2, Developmental Studies Hybridoma Bank (DSHB); 1:100], neurofilament H (clone SMI 312, 801701, BioLegend; 1:50), tetramethylrhodamine-conjugated α-bungarotoxin (T0195, Merck-Sigma; 2 μg/ml), neurofilament 200 (AB5539, Millipore; 1:1000), and synaptophysin (ab130436, Abcam; 1:500). The following secondary antibodies were used: anti-mouse polyclonal goat horseradish peroxidase (HRP) (Dako; 1:2000), anti-rabbit HRP, polyclonal swine (Dako; 1:2000), IRDye 680 anti-mouse (925-68070, LI-COR; 1:20,000), IRDye 800 anti-mouse (925-32210, LI-COR; 1:20,000), IRDye 680 anti-rabbit (926-68073, LI-COR; 1:20,000), IRDye 800 anti-rabbit (925-32211, LI-COR; 1:20,000), and IRDye 680 anti-rat (925-32211, LI-COR; 1:20,000). For immunofluorescence analysis of tissue or cell cultures, Alexa Fluor 488 anti-mouse (A21202), Alexa Fluor 568 anti-mouse (A11004), Alexa Fluor 647 anti-mouse (A21236), Alexa Fluor 488 anti-rabbit (A21206), Alexa Fluor 488 α-bungarotoxin (B13422), Alexa Fluor 647 anti-rabbit (A21244), and Alexa Fluor 594 anti-chicken (A11039) from Thermo Fisher Scientific were used at 1:500 (tissue) or 1:2000 (cell cultures) dilutions.

Animals

Mice were bred, housed, and studied in the animal research facilities at the University of Barcelona. Animals were provided with food and water ad libitum and maintained in a temperature-controlled environment in a 12-hour/12-hour light-dark cycle. Experiments involving animals were performed in accordance with the European Directive 2010/63/EU and the National Institute of Health guidelines for the care and use of laboratory animals. Experiments were approved by the local ethics committee for animal experimentation of the University of Barcelona (CEEA, Barcelona, Spain) with the exception of in vivo electrophysiology procedures, which were approved by the Ethics Committee on Animal and Human Experimentation of the Universitat Autònoma de Barcelona (Bellaterra, Spain).

Cell culture and transfections

HEK293 [CRL-1573, American Type Culture Collection (ATCC)], HEK293T (CRL-3216, ATCC), Cos-7 (CCL-70, ATCC), MEFs, and MEFs deficient in $G\alpha_q$ and Gα ($G\alpha_q$ KD) (a gift from S. Offermmans, Max-Planck-Institute for Heart and Lung Research, Germany) (*24*) (used for the proteomic analysis that validated the mouse origin of the cells and the absence of $G\alpha_q$ and Gα) were cultured in Dulbecco's modified Eagle's medium (DMEM) (Gibco) supplemented with 10% fetal bovine serum and 2 mM glutamine and maintained at 37°C in a 5% CO incubator. SHSY5Y (CRL-2266, ATCC) cells were cultured in DMEM/F12 medium (Gibco). Cells were tested for mycoplasma by PCR analysis or using EZ-PCR mycoplasma detecting kit (Vitro S.A.). Cells were plated 24 hours before being transfected with FuGENE 6 (Promega) or Lipofectamine 2000 (Life Technologies) according to the manufacturer's guidelines.

Mouse hippocampal cultures were obtained from E15 mouse embryos (OF1, Iffa Credo, Lyon, France) as previously described (*14*). Mouse hippocampal cultures at 4 DIV in neurobasal medium containing 0.59% D-glucose were transfected with Lipofectamine 2000 (Life Technologies) according to the manufacturer's guidelines and imaged at 5 to 6 DIV. Essentially, 2 μg of DNA were complexed with 2 μl of Lipofectamine 2000 for 20 min before the mix was added to the medium. The medium was replaced after 30 min, and the cells were cultured for an additional 1 to 3 days. The combinations of plasmids used for neuronal transfections were as follows: (i) pmitoGFP and pAAV-hSyn-hM3D($G\alpha_q$)-mCherry (for stimulation of DREADDs); (ii) pEGFP- and pIRES-containing vectors expressing mitoDsRed (for $G\alpha_q$ expression experiments with bicistronic vectors); (iii) pmitoDsRed and pEGFP- or pEGFP-$G\alpha_q$–containing vectors; or (iv) pmitoDsRed and SCR; pmitoDsRed, pEGFP, and pLKO1-shGq ($G\alpha_q$ KD 1); or pmitoDsRed and pLKO.3G shGq ($G\alpha_q$ KD 2).

Immunoprecipitation and Western blot analyses

For coimmunoprecipitation experiments, whole-cell lysates were prepared in lysis buffer. Lysis buffer contained 50 mM tris-HCl (pH 7.5), 150 mM NaCl, 5 mM EDTA, 1% Triton X-100, 10% glycerol, 10 mM NaF, 50 mM NaHPO7, and 1.5 mM MgCl with protease inhibitors. For dynein assays, lysis buffer contained 25 mM Hepes (pH 7.4), 50 mM potassium acetate, 2 mM magnesium acetate, 0.2% Triton X-100, 1 mM EGTA, 50 mM Mg–adenosine 5′-triphosphate, 10% glicerol, 50 mM NaF, and 1 mM dithiothreitol (DTT). For Ca^{2+} experiments, EDTA was omitted from the lysis buffer, and extracts were split in two before the addition of 2 mM CaCl to one half). Whole-cell lysates were centrifuged, and supernatants were incubated with gentle rocking with a specific antibody (1 to 5 μg) and 1.5 μg of immunoglobulin G (IgG)–free bovine serum albumin (BSA) (MilliporeSigma) for 3 hours or overnight at 4°C. Protein G or protein A Sepharose beads (10 to 20 μg; Merck-Sigma) were added to capture antibodies. When using a bead-Trap–conjugated antibody (anti-Myc and anti-GFP TRAP, ChromoTek) or antibodies conjugated to protein G agarose beads (anti-HA Sepharose beads, Merck-Sigma), 4 to 10 μl of antibody beads were added per sample and incubated for 1 to 2 hours at 4°C. The Bio-Rad protein assay (Bio-Rad) was used to quantify protein in lysates. Samples were rinsed with washing buffer [10 mM tris-HCl (pH 8.0), 300 mM NaCl, 1 mM EDTA, 1 mM EGTA, 1% Triton X-100, 0.5% NP-40, and 1.5 μM MgCl] and resolved by SDS–polyacrylamide gel electrophoresis (PAGE) before being transferred to Immobilon-FL membranes (Millipore). Membranes were incubated with anti-mouse or anti-rabbit antibodies (IRDye 680 and IRDye 800) diluted 1:20,000 in Odyssey blocking buffer (LI-COR). Labeling was visualized with an Odyssey infrared scanner (LI-COR). For quantification, Image Studio software (LI-COR) was used to determine the integrated optic density, and values were normalized to the loading control. Data were normalized to the loading controls Hsp90 or GAPDH. For the proteomic analysis, normal horse serum (NHS)–activated magnetic beads from Pierce (Thermo Fisher Scientific) were used with two different antibodies (C-19 and E-17, Santa Cruz Biotechnology) and mitochondria-enriched cell lysates (*94*) from WT MEFs, $G\alpha_q$ and Gα KO MEFs, and $G\alpha_q$ and Gα KO MEFs stably expressing $G\alpha_q$ and NIH 3T3 cells. Proteins were eluted in ultrapure water and sent for MS analysis (Proteomic Unit CNIC).

GST pull-down assay

GST and GST-fusion proteins were transformed into the *Escherichia coli* strain BL21 and purified with glutathione beads (GE Healthcare). GST proteins in 50 mM tris-HCl (pH 7.5), 150 mM NaCl, 1 mM NP-40, 0.25% deoxycholate, 1 mM EGTA (pH 8.0), and 1 mM NaF were incubated with lysates of SHSY5Y cells (around 1.5 mg of protein) or HEK293T cells transiently transfected with the plasmids indicated in each figure (700 μg of protein lysates) with gentle

rotation for 1 hour at 4°C. Samples were rinsed four times with wash buffer, analyzed by SDS-PAGE, and visualized by either Odyssey analysis or ponceau (Merck-Sigma) staining. In pull-down experiments with purified components, 10 μg of the bead-conjugated GST-Alex3 protein was incubated with 10 ng of purified $G\alpha_q$ in 1 ml of incubation buffer (100 mM NaCl, 20 mM Hepes, 2 mM MgCl, 0.5 mM EDTA, and 1 mM DTT).

Imaging of fixed cells

For hippocampal neurons, cells were seeded on 35-mm, glass-bottom dishes or on 1.5-mm coverslips, fixed with 4% paraformaldehyde (PFA) in phosphate-buffered saline (PBS) for 15 min, washed three times with PBS, and blocked in a solution containing 1% BSA and 0.1% Triton X-100 in PBS. Cells were incubated for 1 hour with primary antibodies at the appropriate dilution in blocking buffer, then washed three to five times with PBS before being incubated with the corresponding secondary antibody at room temperature, washed four times in PBS, and mounted on ProLong Diamond (Invitrogen). Secon dary antibodies (Alexa Fluor 488–, Alexa Fluor 555–, and Alexa Fluor 657–conjugated, Life Technologies) were used at a 1:2000 dilution. Otherwise, cells or neurons expressing $G\alpha_q$ constructs or the indicated plasmids (Miro1-Cherry, Alex3-GFP, and Tom20-Cherry) as indicated in the figures were incubated with or without MitoTracker Red CMXRos before fixation or with antibodies for Tom20 and $G\alpha_q$, Alex3, and the corresponding secondary antibodies as indicated. Images of fixed cultures were taken on a LSM700 confocal microscope (Zeiss) using a 40× [numerical aperture (NA) 1.3] or 63× (NA 1.4) oil immersion objective. For the colocalization analysis in Cos-7 cells and hippocampal neurons, Mander's coefficient with threshold was calculated for each image using defined regions of interest (ROIs) (11 μm) and the JACoP plugin from ImageJ. Images were taken on a LSM700 confocal microscope (Zeiss) using 63× oil objective (NA 1.4).

In vivo imaging of hippocampal neurons

Mouse hippocampal neurons transfected at 4 DIV were imaged in vivo at 5 to 6 DIV. For mitochondrial tracking experiments, an image of the neuron was acquired at a 2048 pixel–by–2048 pixel resolution for subsequent analysis of morphology and localization of the area to be imaged in the axon, and, subsequently, an axonal segment located ~90- to 160-μm distal to the soma was blindly selected and imaged. *Z* stacks of seven images from the axonal region were taken every 6 s during 10 or 15 min using the mitoDsRed channel with an 800 pixel–by–100 pixel resolution and an extra 2× digital zoom. For studies with DREADD receptors or GFP-synaptophysin, mitochondria or synaptophysin-containing vesicles were imaged using the GFP channel. Movies were processed using ImageJ software, and kymographs were generated by tracing the *z*-projections of axons. In kymographs, straight vertical lines were considered to be static mitochondria, and motile mitochondria (nonstraight vertical lines) were traced to evaluate their motility and directionality (*45*, *95*, *96*). The percentage of time in motion was calculated as the percentage of time a given mitochondrion (static or motile) spent moving at a speed over 0.0083 μm/s in the anterograde or retrograde directions. The percentage of motile mitochondria represents the relation between number of motile and total mitochondria for each condition. In control neurons, a similar fraction of anterograde and retrograde movement is normally observed. The percentage of mitochondria in movement (20 to 30%) and the average velocity (between 0.3 and 0.7 μm/s) also agreed with previous studies, which supports the validity of the methodology used in this study (*3*). In vitro imaging experiments were performed at 37°C in an atmosphere of 5% CO with a LSM780 confocal microscope (Zeiss) equipped with 40× (NA 1.3) and 63× (NA 1.4) oil immersion objectives. Electronics were controlled through the ZEN software (Zeiss).

Enhanced resolution confocal microscopy

Cos-7 cells were transfected with $G\alpha_q$ and/or pCDH-DsRed-Miro1/GFP-Miro1/Tom20-Cherry or GFP-Alex3 and fixed with 3.7% formaldehyde after 24 hours and permeabilized with 1% Triton X-100 and 0.1% sodium deoxycholate. Cells were blocked with 5% goat serum/0.1% BSA and stained with combinations of the following antibodies: anti–Cox IV (459600/C0941, Life Technologies), anti-$G\alpha_q$ (C-19, BD Biosciences or Santa Cruz Biotechnology), or anti-Alex3 (ProteinTech). Alexa Fluor 568 anti-mouse, Alexa Fluor 488 anti-rabbit mouse, or Alexa Fluor 647 anti-rabbit IgGs were used as secondary antibodies. Antibodies used for immunofluorescence (primary and secondary) were tested for specificity using the corresponding KO MEFs and/or cells overexpressing the target proteins. Coverslips were mounted with ProLong Diamond. Cells were blindly selected, and image acquisition was performed using an N-SIM (super-resolution microscope system) (Nikon) equipped with a super-resolution Apo total internal reflection fluorescence 100× (NA 1.49) objective and a DU897 Ixon camera (Andor Technologies). Three-dimensional SIM image stacks were acquired with a *Z* distance of 0.15 μm. Raw images were computationally reconstructed using the reconstruction slice system from NIS-Elements software (Nikon) while keeping the same parameters. Other images were taken with a Zeiss LSM780 system equipped with a 63× (NA 1.4) objective.

Neuronal and cell treatments

In live imaging experiments using the $G\alpha_q$-specific inhibitor, neurons transfected with the plasmids of interest were incubated with 10 μM YM-254890 (Focus Biomolecules) for 30 min before imaging, as previously reported (*35*, *97*). In GPCR activation assays, neurons were cotransfected with mitoGFP and with a Cherry-tagged hM3D ($G\alpha_q$) DREADD receptor (*98*). Twenty-four hours after transfection, axons of $G\alpha_q$-DREADD–expressing neurons were imaged before and 15 min after the addition of 1 μM CNO (Tocris). For IP3 receptor inhibitor treatment, neurons transfected with the plasmids of interest [internal ribosomal entry site (IRES) vectors] were incubated with 4 μM xestospongin C (Tocris) or dimethyl sulfoxide for 1 hour before being imaged in vivo. To measure fluctuations in mitochondrial membrane potential, HEK293 cells or hippocampal neurons expressing GFP vectors with the different forms of $G\alpha_q$ were incubated with 200 nM MitoTracker Red CMXRos (Thermo Fisher Scientific) for 30 min at 37°C before fixation. Cells were blindly selected and imaged with a LSM780 confocal microscope (Zeiss) equipped with a 63× (NA 1.4) oil immersion objective. Confocal images in the green and red channels were acquired, and the intensity of red fluorescence was analyzed with the NeuronJ plugin from the ImageJ software. The fluorescence signal was determined for each cell and averaged.

Generation of a CNS-specific Alex3 KO mice

To generate a CNS-specific Alex3 conditional knockout line, *Armcx3*$^{fl/fl}$ female mice (*15*) were mated with *Nestin-Cre*$^{+/-}$ males (*99*), which express the Cre recombinase under the control of the *Nestin* promoter. All mice were kept in a C57/Bl6 background. The following

experimental groups were obtained: *A* (*Armcx3*$^{+/+}$ females, 25%), *B* (*Armcx3*$^{+/+}$ males, 25%), *C* (*Armcx3* females, 25%), and *D* (*Armcx3*$^{-/-}$ males, Alex3 KO, 25%). Unless otherwise stated, *B* males and *A* females were used interchangeably as controls. Because of the crossing strategy used and the location of *Armcx3* in the X chromosome, all Alex3 CKO mice used for experiments were males. Mating day was considered as E0 and the day of birth as P0. Mice were studied at E14 or P5 to P10.

Genotyping

Mice were genotyped using two complementary PCRs on genomic DNA extracted from tails. To detect floxed Alex3, the following primers were used: *Armcx3S1F*, 5′-GGGGCGGTGGGCAGGATGACAG-3′; *Armcx3 S4F*, 5′-AAGTTCTAGGAATCGAGAGCC-3′; *Armcx3 S*, 5′-ATCATTTCCCCTTGACTCTGG-3′. To detect the *Nestin-Cre* allele, the following primers were used: WT-Cre, 5′-CTAGGCCACGAATTGAAAGATCT-3′ (forward) and 5′-GTAGGTGGAAATTCTAGCATCATCC-3′ (reverse); Cre, 5′-GCGGTCTGGCAGTAAAAACTATC-3′ (forward) and 5′-GTGAAACAGCATTGCTGTCACTT-3′ (reverse).

Behavioral phenotyping

Behavioral tests were performed in mice to assess their general neuromuscular function, body muscle strength, and posture. Mice were analyzed at P6 to P8. Phenotyping included body weight measurement, hind limb clasping tube test, hind limb suspension test, and kyphosis evaluation. Performance for each measure was recorded on a scale of 0 to 4 as previously described (*100*, *101*).

Tissue processing and histology

Postnatal mice were anesthetized with isofluorane and perfused with 4% PFA in 0.1 M phosphate buffer (PB). Brains and spinal cords were extracted, postfixed overnight with 4% PFA in PB, cryoprotected with 30% sucrose in PBS, and frozen at −42°C in isopentane. Frozen brain and cerebellar samples were sectioned in 50-μm coronal or sagittal sections, using a freezing microtome (Leica). Spinal cord samples were sectioned in a cryostat (Leica), either at 16 μm and collected in slides or at 30 μm and stored in cryoprotectant solution (85% glycerol, 100% ethylene glycol, 0.1 M PBS), and kept at −20°C until use. In addition, intact (whole mount) diaphragms were obtained to assess neuromuscular synapses. The gastrocnemius muscles were harvested after perfusion, cryopreserved in PBS–30% sucrose, and sectioned in 60-μm-thick sections. The overall histological structure, width, and length of several brain regions were assessed using Nissl and/or 4′,6-diamidino-2-phenylindole (DAPI) staining.

For chromogenic immunodetection of antigens, sections were incubated with 10% methanol and 3% HO in PB and blocked for 2 hours with 10% of either normal goat serum (NGS) or NHS, 0.3% Triton X-100, and, when needed, anti-mouse IgG F(ab′)2 fragment (Jackson ImmunoResearch; 1:300) in 0.2% gelatin-PBS. Sections were incubated with primary antibodies overnight at 4°C in 5% NGS/NHS and 0.3% Triton X-100 in PBS–0.2% gelatin. Section were sequentially incubated with biotinylated secondary antibodies (1:200; 2 hours at room temperature) and streptavidin-HRP (1:400; 2 hours at room temperature), each of them diluted in 5% NGS/NHS and 0.3% Triton X-100 in PBS–0.2% gelatin. Bound antibodies were visualized using 0.03% diaminobenzidine and 0.006% HO in PB as peroxidase substrates. Sections were mounted on gelatinized slides, dehydrated, and coverslipped with Eukitt (Merck-Sigma).

For immunofluorescence, frozen brain sections were permeabilized as above. To detect CTIP2 or Cux1, heat-mediated antigen retrieval was performed before blocking. Primary antibodies were detected using appropriate secondary antibodies (Alexa Fluor, Invitrogen; 1:500). Nuclei were stained using DAPI (1:200), and sections were mounted in Mowiol (Calbiochem). For neuromuscular synapse staining, diaphragms samples were permeabilized in 0.5% Triton X-100 in PBS and blocked in 10% donkey serum in 0.1 M PBS for 1 hour at room temperature before being incubated with primary antibodies against the synaptic vesicle protein SV2A and neurofilament H (clone SMI 312) for 2 days at 4°C. After several washes in 0.5% Triton X-100 and 1% donkey serum in 0.1 M PBS, samples were incubated overnight with Alexa Fluor 488 donkey anti-mouse secondary antibody and tetramethylrhodamine-conjugated α-bungarotoxin in 0.1 M PBS. Samples were washed in 0.5% Triton X-100, 1% donkey serum in 0.1 M PBS, and whole-mounted in ProLong Gold (Invitrogen) or Mowiol medium (Merck-Sigma). Frozen gastrocnemius muscle sections were incubated with neurofilament 200 (Millipore) and synaptophysin (Abcam) primary antibodies for 48 hours at 4°C. Sections were then incubated overnight with Alexa Fluor 594 (Invitrogen; 1:200) and Alexa Fluor 488 α-bungarotoxin (Life Technologies; 1:150). Sections were mounted with Fluoromount G (Southern Biotech).

Image acquisition and analysis of Alex3 CKO tissue

Bright-field images were captured with a digital DP72 camera (Olympus) attached to an ECLIPSE 600 (Nikon) optical microscope with Olympus Cell F software and with a NanoZoomer 2.0-HT (Hamamatsu Photonics). Immunofluorescence images were acquired with either an ECLIPSE E1000 (Nikon) optical microscope combined with a Cool SNAP camera or with SPE (Leica) or TCS SP2 (Leica) confocal microscopes.

Low-magnification (2×) images of DAPI-stained sections were used to measure the maximum width and length of the brain hemispheres at bregma positions ranging from +4.11 to +4.95 mm (*102*) using ImageJ (Fiji) software. In addition, the width of the primary somatosensory cortex was also measured using 10× images of DAPI-stained sections. Images of Nissl-stained cerebellar sections from P10 mice were used to measure the maximum length of lobules IIc, IIIa, III, and IV.

To determine the number and morphology of Purkinje cells, P10 cerebellar sections were stained with anti-calbindin antibody. The number, cell body size, and dendritic tree width (in the molecular layer) of Purkinje cells were analyzed. To assess cell death and microgliosis, P5 brain sections were stained with antibodies against either the cleaved form of caspase-3 or Iba-1, respectively. Several brain regions were assessed, including cortex (layers II, III, and V), striatum, subiculum, and dentate gyrus. In each region, the number of cells with positive staining within a defined area was counted and expressed as the number of positive cells per square millimeter. The number of spinal ventral horn motor neurons was determined by counting the ChAT-positive cells that contained a clearly visible nucleus in serial P5 thoracic spinal cord sections.

Intact (whole mount) diaphragms from four or five P6 mice per geno type were used to image neuromuscular synapses. Muscle preparations were visualized using a laser scanning confocal microscope LSM900 and Zen software (Zeiss). Neuromuscular synapses from three regions across the diaphragm were assessed in each preparation. For presynaptic analyses, endplates were categorized as either vacant (no neurofilament H or

SV2 overlapping the endplate) or fully occupied (neurofilament H or SV2 overlapping more than 80% of the endplate). The synaptic density and the percentage of fully occupied endplates were calculated. The density of NMJs in gastrocnemius muscles in defined areas was counted similarly using *z*-stack images acquired in a Leica Thunder microscope.

Motor nerve conduction tests

Motor nerve conduction tests were performed stimulating the sciatic nerve through a pair of needle electrodes placed at the sciatic notch. The CMAP was recorded from the gastrocnemius muscle with microneedle electrodes (*103*). Potentials were amplified and displayed on a digital oscilloscope (Tektronix 450S), and the amplitude and latency were determined. During the tests, the body temperature of the mice was maintained between 34° and 36°C on a heating pad.

Sholl and mitochondrial Sholl analysis

To prepare samples for arborization analyses, fixed neuronal cultures were permeabilized with 0.1% Triton X-100 in PBS for 5 min, blocked with 10% serum in PBS, and incubated in 5% serum overnight with anti-GFP antibody. Images were taken with a LSM780 (Zeiss) confocal microscope equipped with a 20× objective. Images from live neuronal cultures blindly selected were acquired on a LSM780 (Zeiss) upright confocal microscope equipped with a 63× (NA 1.4) or a 40× (NA 1.3) oil immersion objective (2048 pixel–by–2048 pixel resolution).

Some images were stitched together using Zen software (Zeiss) to allow visualization of the entire dendritic arbor. Dendrites were traced using NeuronJ plugin from ImageJ software to quantify dendrite number and length and number of branching points and to perform Sholl analysis. Mitochondrial Sholl analysis was performed using a custom ImageJ plugin as previously described (*45*), which quantified the amount of mitoDsRed pixels within shells radiating out from the soma at 1-pixel intervals. The density of the mitochondria in the soma (mitochondrial area/cell body area) was calculated using the ImageJ integrated density of mitoDsRed pixels after subtraction of the integrated density of the nuclei in the red channel.

Mitochondrial number and length

Mitochondrial number and length were determined from axonal proximal segments of 25 to 40 neurons per condition. Live neuronal cultures expressing mitoDsRed were imaged with a LSM780 (Zeiss) confocal microscope equipped with 40× (NA 1.3) and 63× (NA 1.4) oil immersion objectives. Confocal images of the red (mtDsRed) channel were acquired and analyzed with the NeuronJ plugin of ImageJ software. The number of mitochondria within axons was quantified and standardized to the length of the axonal section imaged, with axonal and mitochondrial length determined using the segmented line tool.

Tissue processing and Western blot analysis of Alex3 CKO mice

Brains and spinal cords were dissected from E14 and P5 to P7 mice, frozen in liquid nitrogen, and stored at −80°C before processing. Frozen tissue was lysed using a power homogenizer (Polytron) in 10 vol of radioimmunoprecipitation assay lysis buffer (50 mM tris-HCl, 150 mM NaCl, 1 mM EDTA, 0.5% sodium deoxycholate, 0.1% SDS, and 1% Triton X-100) containing CompleteMini protease inhibitor cocktail (Roche) and phosphatase inhibitors (10 mM tetrasodium pyrophosphate, 200 μM sodium orthovanadate, and 10 mM sodium fluoride). Lysates were centrifuged, and supernatants were collected and stored at −80°C. Bicinchoninic acid (BCA) protein assay (Thermo Fisher Scientific) was used for protein quantification.

Brain and spinal cord protein samples were resolved on SDS-PAGE and transferred onto nitrocellulose membranes. Membranes were blocked in 5% nonfat milk powder in TBS-T [10 mM tris (pH 7.4), 140 mM NaCl, and 1% Tween 20) and incubated with the primary antibodies overnight at 4°C. For chemiluminescent detection, membranes were incubated with secondary HRP-labeled antibodies (HRP anti-mouse (polyclonal goat, Dako; 1:2000) and HRP anti-rabbit (polyclonal swine, Dako; 1:2000) diluted in 5% nonfat milk TBS-T or 1% BSA tris-buffered saline and subsequently developed with the enhanced chemiluminesence system (GE Healthcare). Bands were quantified by densitometry using Gel Pro software and were normalized to the loading control.

Genetic variant analysis of *ARMCX3*

Genetic variants; loss-of-function mutations; allelic frequency (see table S1) of *ARMCX3;* the flanking genes *NRNPH2*, *ARCMX4*, *ARMCX1*, *ACRMCX6*, *ARMCX2*, *ZMAT1*, and *ARMCX5*, per order in human chromosome X, as well as *RHOT1*, *RHOT2*, and *TRAK2* in control populations were assessed in VARSOME (https://varsome.com/). Involvement in Mendelian diseases was determined in Human Mutation Gene Database and, in pathogenic structural rearrangements, was consulted in ClinVar (table S1).

Statistical analyses

Excel (Microsoft), GraphPad Prism (GraphPad), and SPSS Statistics (SPSS) software were used to analyze the data. Unpaired Student's *t* test (with Welch correction when appropriate) or Mann-Whitney *U* test were used to test differences between two conditions. Comparison of multiple conditions was performed by one-way analysis of variance (ANOVA) with Bonferroni post hoc test for parametric data or by Kruskal-Wallis test, followed by Dunn's multiple comparison test for nonparametric data. For brain width and height measurements, general estimated equations for repeated measures analysis were performed using the SPSS software. Statistical significance was set at $P < 0.05$ and represented as $^{*}P < 0.05$, $^{**}P < 0.01$, $^{***}P < 0.001$, and $^{****}P < 0.0001$. Values are given as means ± SEM.

Supplementary Materials

This PDF file includes:

Figs. S1 to S9
Table S1

Other Supplementary Material for this manuscript includes the following:

MDAR Reproducibility Checklist

REFERENCES AND NOTES

1. A. F. MacAskill, J. T. Kittler, Control of mitochondrial transport and localization in neurons. *Trends Cell Biol.* **20**, 102–112 (2010).
2. N. Birsa, R. Norkett, N. Higgs, G. Lopez-Domenech, J. T. Kittler, Mitochondrial trafficking in neurons and the role of the Miro family of GTPase proteins. *Biochem. Soc. Trans.* **41**, 1525–1531 (2013).
3. T. L. Schwarz, Mitochondrial trafficking in neurons. *Cold Spring Harb. Perspect. Biol.* **5**, a011304 (2013).
4. X. Wang, T. L. Schwarz, The mechanism of Ca^{2+}–dependent regulation of kinesin-mediated mitochondrial motility. *Cell* **136**, 163–174 (2009).

5. M. Saotome, D. Safiulina, G. Szabadkai, S. Das, A. Fransson, P. Aspenstrom, R. Rizzuto, G. Hajnoczky, Bidirectional Ca^{2+}–dependent control of mitochondrial dynamics by the Miro GTPase. *Proc. Natl. Acad. Sci.* **105**, 20728–20733 (2008).
6. A. F. MacAskill, J. E. Rinholm, A. E. Twelvetrees, I. L. Arancibia-Carcamo, J. Muir, A. Fransson, P. Aspenstrom, D. Attwell, J. T. Kittler, Miro1 Is a calcium sensor for glutamate receptor-dependent localization of mitochondria at synapses. *Neuron* **61**, 541–555 (2009).
7. V. Costa, L. Scorrano, Shaping the role of mitochondria in the pathogenesis of Huntington's disease. *EMBO J.* **31**, 1853–1864 (2012).
8. P. Jadiya, D. W. Kolmetzky, D. Tomar, A. Di Meco, A. A. Lombardi, J. P. Lambert, T. S. Luongo, M. H. Ludtmann, D. Praticò, J. W. Elrod, Impaired mitochondrial calcium efflux contributes to disease progression in models of Alzheimer's disease. *Nat. Commun.* **10**, 3885 (2019).
9. M. Calvo-Rodriguez, S. S. Hou, A. C. Snyder, E. K. Kharitonova, A. N. Russ, S. Das, Z. Fan, A. Muzikansky, M. Garcia-Alloza, A. Serrano-Pozo, E. Hudry, B. J. Bacskai, Increased mitochondrial calcium levels associated with neuronal death in a mouse model of Alzheimer's disease. *Nat. Commun.* **11**, 2146 (2020).
10. X. Cen, Y. Chen, X. Xu, R. Wu, F. He, Q. Zhao, Q. Sun, C. Yi, J. Wu, A. Najafov, H. Xia, Pharmacological targeting of MCL-1 promotes mitophagy and improves disease pathologies in an Alzheimer's disease mouse model. *Nat. Commun.* **11**, 5731 (2020).
11. H. Meng, C. Yamashita, K. Shiba-Fukushima, T. Inoshita, M. Funayama, S. Sato, T. Hatta, T. Natsume, M. Umitsu, J. Takagi, Y. Imai, N. Hattori, Loss of Parkinson's disease-associated protein CHCHD2 affects mitochondrial crista structure and destabilizes cytochrome c. *Nat. Commun.* **8**, 15500 (2017).
12. J. Kaeffer, G. Zeder-Lutz, F. Simonin, S. Lecat, GPRASP/ARMCX protein family: Potential involvement in health and diseases revealed by their novel interacting partners. *Curr. Top. Med. Chem.* **21**, 227–254 (2021).
13. F. Simonin, P. Karcher, J. J.-M. Boeuf, A. Matifas, B. L. Kieffer, Identification of a novel family of G protein-coupled receptor associated sorting proteins. *J. Neurochem.* **89**, 766–775 (2004).
14. G. López-Doménech, R. Serrat, S. Mirra, S. D'Aniello, I. Somorjai, A. Abad, N. Vitureira, E. García-Arumí, M. T. Alonso, M. Rodriguez-Prados, F. Burgaya, A. L. Andreu, J. García-Sancho, R. Trullas, J. Garcia-Fernàndez, E. Soriano, The Eutherian Armcx genes regulate mitochondrial trafficking in neurons and interact with Miro and Trak2. *Nat. Commun.* **3**, 814 (2012).
15. S. Mirra, A. Gavaldà-Navarro, Y. Manso, M. Higuera, R. Serrat, M. T. Salcedo, F. Burgaya, J. M. Balibrea, E. Santamaría, I. Uriarte, C. Berasain, M. A. Avila, B. Mínguez, E. Soriano, F. Villarroya, ARMCX3 mediates susceptibility to hepatic tumorigenesis promoted by dietary lipotoxicity. *Cancers* **13**, 1110 (2021).
16. R. Serrat, S. Mirra, J. Figueiro-Silva, E. Navas-Pérez, M. Quevedo, G. López-Doménech, P. Podlesniy, F. Ulloa, J. Garcia-Fernàndez, R. Trullas, E. Soriano, The Armc10/SVH gene: Genome context, regulation of mitochondrial dynamics and protection against Aβ-induced mitochondrial fragmentation. *Cell Death Dis.* **5**, e1163–e1163 (2014).
17. R. Cartoni, M. W. Norsworthy, F. Bei, C. Wang, S. Li, Y. Zhang, C. V. Gabel, T. L. Schwarz, Z. He, The mammalian-specific protein armcx1 regulates mitochondrial transport during axon regeneration. *Neuron* **92**, 1294–1307 (2016).
18. R. Irannejad, M. von Zastrow, GPCR signaling along the endocytic pathway. *Curr. Opin. Cell Biol.* **27**, 109–116 (2014).
19. Y.-J. I. Jong, S. K. Harmon, K. L. O'Malley, Intracellular GPCRs play key roles in synaptic plasticity. *ACS Chem. Nerosci.* **9**, 2162–2172 (2018).
20. G. Sánchez-Fernández, S. Cabezudo, C. García-Hoz, C. Benincá, A. M. Aragay, F. Mayor, C. Ribas, $G\alpha_q$ signalling: The new and the old. *Cell. Signal.* **26**, 833–848 (2014).
21. E. Hebert-Chatelain, T. Desprez, R. Serrat, L. Bellocchio, E. Soria-Gomez, A. Busquets-Garcia, A. C. P. Zottola, A. Delamarre, A. Cannich, P. Vincent, M. Varilh, L. M. Robin, G. Terral, M. D. García-Fernández, M. Colavita, W. Mazier, F. Drago, N. Puente, L. Reguero, I. Elezgarai, J.-W. Dupuy, D. Cota, M.-L. Lopez-Rodriguez, G. Barreda-Gómez, F. Massa, P. Grandes, G. Bénard, G. Marsicano, A cannabinoid link between mitochondria and memory. *Nature* **539**, 555–559 (2016).
22. G. Bénard, F. Massa, N. Puente, J. Lourenço, L. Bellocchio, E. Soria-Gómez, I. Matias, A. Delamarre, M. Metna-Laurent, A. Cannich, E. Hebert-Chatelain, C. Mulle, S. Ortega-Gutiérrez, M. Martín-Fontecha, M. Klugmann, S. Guggenhuber, B. Lutz, J. Gertsch, F. Chaouloff, M. L. López-Rodríguez, P. Grandes, R. Rossignol, G. Marsicano, Mitochondrial CB1 receptors regulate neuronal energy metabolism. *Nat. Neurosci.* **15**, 558–564 (2012).
23. D. Jimenez-Blasco, A. Busquets-Garcia, E. Hebert-Chatelain, R. Serrat, C. Vicente-Gutierrez, C. Ioannidou, P. Gómez-Sotres, I. Lopez-Fabuel, M. Resch-Beusher, E. Resel, D. Arnouil, D. Saraswat, M. Varilh, A. Cannich, F. Julio-Kalajzic, I. B.-D. Río, A. Almeida, N. Puente, S. Achicallende, M.-L. Lopez-Rodriguez, C. Jollé, N. Déglon, L. Pellerin, C. Josephine, G. Bonvento, A. Panatier, B. Lutz, P.-V. Piazza, M. Guzmán, L. Bellocchio, A.-K. Bouzier-Sore, P. Grandes, J. P. Bolaños, G. Marsicano, Glucose metabolism links astroglial mitochondria to cannabinoid effects. *Nature* **583**, 603–608 (2020).
24. C. Benincá, J. Planagumà, A. de Freitas Shuck, R. Acín-Perez, J. P. Muñoz, M. M. de Almeida, J. H. Brown, A. N. Murphy, A. Zorzano, J. A. Enríquez, A. M. Aragay, A new non-canonical pathway of $G\alpha_q$ protein regulating mitochondrial dynamics and bioenergetics. *Cell. Signal.* **26**, 1135–1146 (2014).
25. A. L. Frederick, T. P. Saborido, G. D. Stanwood, Neurobehavioral phenotyping of $G\alpha_q$ knockout mice reveals impairments in motor functions and spatial working memory without changes in anxiety or behavioral despair. *Front. Behav. Neurosci.* **6**, 29 (2012).
26. D. L. Graham, M. A. Buendia, M. A. Chapman, H. H. Durai, G. D. Stanwood, Deletion of $G\alpha_q$ in the telencephalon alters specific neurobehavioral outcomes. *Synapse* **69**, 434–445 (2015).
27. S. Offermanns, K. Hashimoto, M. Watanabe, W. Sun, H. Kurihara, R. F. Thompson, Y. Inoue, M. Kano, M. I. Simon, Impaired motor coordination and persistent multiple climbing fiber innervation of cerebellar Purkinje cells in mice lacking $G\alpha_q$. *Proc. Natl. Acad. Sci.* **94**, 14089–14094 (1997).
28. J. Hu, M. Stern, L. E. Gimenez, L. Wanka, L. Zhu, M. Rossi, J. Meister, A. Inoue, A. G. Beck-Sickinger, V. V. Gurevich, J. Wess, A G protein-biased designer G protein-coupled receptor useful for studying the physiological relevance of Gq/11-dependent signaling pathways. *J. Biol. Chem.* **291**, 7809–7820 (2016).
29. B. L. Roth, DREADDs for Neuroscientists. *Neuron* **89**, 683–694 (2016).
30. G. Fan, L. M. Ballou, R. Z. Lin, Phospholipase C-independent activation of glycogen synthase kinase-3β and C-terminal Src kinase by $G\alpha_q$. *J. Biol. Chem.* **278**, 52432–52436 (2003).
31. A. Shankaranarayanan, C. A. Boguth, S. Lutz, C. Vettel, F. Uhlemann, M. Aittaleb, T. Wieland, J. J. G. Tesmer, Galpha q allosterically activates and relieves autoinhibition of p63RhoGEF. *Cell. Signal.* **22**, 1114–1123 (2010).
32. S. Cabezudo, M. Sanz-Flores, A. Caballero, I. Tasset, E. Rebollo, A. Diaz, A. M. Aragay, A. M. Cuervo, F. Mayor, C. Ribas, $G\alpha_q$ activation modulates autophagy by promoting mTORC1 signaling. *Nat. Commun.* **12**, 4540 (2021).
33. Z. J. Wang, F. Zhao, C. F. Wang, X. M. Zhang, Y. Xiao, F. Zhou, M. N. Wu, J. Zhang, J. S. Qi, W. Yang, X. Wang, Xestospongin C, a reversible ip3 receptor antagonist, alleviates the cognitive and pathological impairments in APP/PS1 mice of Alzheimer's disease. *J. Alzheimers Dis.* **72**, 1217–1231 (2019).
34. T. Oka, K. Sato, M. Hori, H. Ozaki, H. Karaki, Xestospongin C, a novel blocker of IP3 receptor, attenuates the increase in cytosolic calcium level and degranulation that is induced by antigen in RBL-2H3 mast cells. *Br. J. Pharmacol.* **135**, 1959–1966 (2002).
35. J. Takasaki, T. Saito, M. Taniguchi, T. Kawasaki, Y. Moritani, K. Hayashi, M. Kobori, A novel $G\alpha_q$/11-selective inhibitor. *J. Biol. Chem.* **279**, 47438–47445 (2004).
36. T. Uemura, T. Kawasaki, M. Taniguchi, Y. Moritani, K. Hayashi, T. Saito, J. Takasaki, W. Uchida, K. Miyata, Biological properties of a specific $G\alpha_q$/11inhibitor, YM-254890, on platelet functions and thrombus formation under high-shear stress. *Br. J. Pharmacol.* **148**, 61–69 (2006).
37. J. Zhang, W. Liu, J. Liu, W. Xiao, L. Liu, C. Jiang, X. Sun, P. Liu, Y. Zhu, C. Zhang, Q. Chen, G-protein β2 subunit interacts with mitofusin 1 to regulate mitochondrial fusion. *Nat. Commun.* **1**, 101 (2010).
38. R. Serrat, G. López-Doménech, S. Mirra, M. Quevedo, J. Garcia-Fernàndez, F. Ulloa, F. Burgaya, E. Soriano, The non-canonical Wnt/PKC pathway regulates mitochondrial dynamics through degradation of the arm-like domain-containing protein Alex3. *PLOS ONE* **8**, e67773 (2013).
39. P. Chan, M. Gabay, F. A. Wright, W. Kan, S. S. Oner, S. M. Lanier, A. V. Smrcka, J. B. Blumer, G. G. Tall, Purification of heterotrimeric G protein α subunits by GST-Ric-8 association. *J. Biol. Chem.* **286**, 2625–2635 (2011).
40. S. Mariggiò, C. García-Hoz, S. Sarnago, A. De Blasi, F. Mayor, C. Ribas, Tyrosine phosphorylation of G-protein-coupled-receptor kinase 2 (GRK2) by c-Src modulates its interaction with $G\alpha_q$. *Cell. Signal.* **18**, 2004–2012 (2006).
41. A. F. MacAskill, T. A. Atkin, J. T. Kittler, Mitochondrial trafficking and the provision of energy and calcium buffering at excitatory synapses. *Eur. J. Neurosci.* **32**, 231–240 (2010).
42. G. López-Doménech, J. H. Howden, C. Covill-Cooke, C. Morfill, J. V. Patel, R. Bürli, D. Crowther, N. Birsa, N. J. Brandon, J. T. Kittler, Loss of neuronal Miro1 disrupts mitophagy and induces hyperactivation of the integrated stress response. *EMBO J.* **40**, e100715 (2021).
43. M. van Spronsen, M. Mikhaylova, J. Lipka, M. A. Schlager, D. J. van den Heuvel, M. Kuijpers, P. S. Wulf, N. Keijzer, J. Demmers, L. C. Kapitein, D. Jaarsma, H. C. Gerritsen, A. Akhmanova, C. C. Hoogenraad, TRAK/Milton motor-adaptor proteins steer mitochondrial trafficking to axons and dendrites. *Neuron* **77**, 485–502 (2013).
44. D. Srivastava, L. Gakhar, N. O. Artemyev, Structural underpinnings of Ric8A function as a G-protein α-subunit chaperone and guanine-nucleotide exchange factor. *Nat. Commun.* **10**, 3084 (2019).
45. G. López-Doménech, N. F. Higgs, V. Vaccaro, H. Roš, I. L. Arancibia-Cárcamo, A. F. MacAskill, J. T. Kittler, Loss of dendritic complexity precedes neurodegeneration in a mouse model with disrupted mitochondrial distribution in mature dendrites. *Cell Rep.* **17**, 317–327 (2016).
46. N. Wettschureck, A. Moers, B. Wallenwein, A. F. Parlow, C. Maser-Gluth, S. Offermanns, Loss of $G_{q/11}$ family G proteins in the nervous system causes pituitary somatotroph hypoplasia and dwarfism in mice. *Mol. Cell. Biol.* **25**, 1942–1948 (2005).
47. G. J. Russo, K. Louie, A. Wellington, G. T. Macleod, F. Hu, S. Panchumarthi, K. E. Zinsmaier, *Drosophila* Miro is required for both anterograde and retrograde axonal mitochondrial transport. *J. Neurosci.* **29**, 5443–5455 (2009).

48. E. E. Glater, L. J. Megeath, R. S. Stowers, T. L. Schwarz, Axonal transport of mitochondria requires milton to recruit kinesin heavy chain and is light chain independent. *J. Cell Biol.* **173**, 545–557 (2006).
49. K. Brickley, M. J. Smith, M. Beck, F. A. Stephenson, GRIF-1 and OIP106, members of a novel gene family of coiled-coil domain proteins. *J. Biol. Chem.* **280**, 14723–14732 (2005).
50. Å. Fransson, A. Ruusala, P. Aspenström, The atypical Rho GTPases Miro-1 and Miro-2 have essential roles in mitochondrial trafficking. *Biochem. Biophys. Res. Commun.* **344**, 500–510 (2006).
51. S. Rosciglione, C. Thériault, M.-O. Boily, M. Paquette, C. Lavoie, Gαs regulates the post-endocytic sorting of G protein-coupled receptors. *Nat. Commun.* **5**, 4556 (2014).
52. B. F. Krakstad, V. V. Ardawatia, A. M. Aragay, A role for Galpha12/Galpha13 in p120ctn regulation. *Proc. Natl. Acad. Sci. U.S.A.* **101**, 10314–10319 (2004).
53. V. V. Ardawatia, M. Masià-Balagué, B. F. Krakstad, B. B. Johansson, K. M. Kreitzburg, E. Spriet, A. E. Lewis, T. E. Meigs, A. M. Aragay, Gα(12) binds to the N-terminal regulatory domain of p120(ctn), and downregulates p120(ctn) tyrosine phosphorylation induced by Src family kinases via a RhoA independent mechanism. *Exp. Cell Res.* **317**, 293–306 (2011).
54. N. Nemani, E. Carvalho, D. Tomar, Z. Dong, A. Ketschek, S. L. Breves, F. Jaña, A. M. Worth, J. Heffler, P. Palaniappan, A. Tripathi, R. Subbiah, M. F. Riitano, A. Seelam, T. Manfred, K. Itoh, S. Meng, H. Sesaki, W. J. Craigen, S. Rajan, S. Shanmughapriya, J. Caplan, B. L. Prosser, D. L. Gill, P. B. Stathopulos, G. Gallo, D. C. Chan, P. Mishra, M. Madesh, MIRO-1 determines mitochondrial shape transition upon GPCR activation and Ca^{2+} stress. *Cell Rep.* **23**, 1005–1019 (2018).
55. M. V. Hinrichs, M. Torrejón, M. Montecino, J. Olate, Ric-8: Different cellular roles for a heterotrimeric G-protein GEF. *J. Cell. Biochem.* **113**, 2797–2805 (2012).
56. Z. Chen, C. Lei, C. Wang, N. Li, M. Srivastava, M. Tang, H. Zhang, J. M. Choi, S. Y. Jung, J. Qin, J. Chen, Global phosphoproteomic analysis reveals ARMC10 as an AMPK substrate that regulates mitochondrial dynamics. *Nat. Commun.* **10**, 104 (2019).
57. E. L. Huttlin, L. Ting, R. J. Bruckner, F. Gebreab, M. P. Gygi, J. Szpyt, S. Tam, G. Zarraga, G. Colby, K. Baltier, R. Dong, V. Guarani, L. P. Vaites, A. Ordureau, R. Rad, B. K. Erickson, M. Wühr, J. Chick, B. Zhai, D. Kolippakkam, J. Mintseris, R. A. Obar, T. Harris, S. Artavanis-Tsakonas, M. E. Sowa, P. De Camilli, J. A. Paulo, J. W. Harper, S. P. Gygi, The bioplex network: A systematic exploration of the human interactome. *Cell* **162**, 425–440 (2015).
58. E. L. Huttlin, R. J. Bruckner, J. Navarrete-Perea, J. R. Cannon, K. Baltier, F. Gebreab, M. P. Gygi, A. Thornock, G. Zarraga, S. Tam, J. Szpyt, B. M. Gassaway, A. Panov, H. Parzen, S. Fu, A. Golbazi, E. Maenpaa, K. Stricker, S. Guha Thakurta, T. Zhang, R. Rad, J. Pan, D. P. Nusinow, J. A. Paulo, D. K. Schweppe, L. P. Vaites, J. W. Harper, S. P. Gygi, Dual proteome-scale networks reveal cell-specific remodeling of the human interactome. *Cell* **184**, 3022–3040.e28 (2021).
59. A. Belous, A. Wakata, C. D. Knox, I. B. Nicoud, J. Pierce, C. D. Anderson, C. W. Pinson, R. S. Chari, Mitochondrial P2Y-Like receptors link cytosolic adenosine nucleotides to mitochondrial calcium uptake. *J. Cell. Biochem.* **92**, 1062–1073 (2004).
60. Q. Wang, H. Zhang, H. Xu, D. Guo, H. Shi, Y. Li, W. Zhang, Y. Gu, 5-HTR3 and 5-HTR4 located on the mitochondrial membrane and functionally regulated mitochondrial functions. *Sci. Rep.* **6**, 37336 (2016).
61. F. Gbahou, E. Cecon, G. Viault, R. Gerbier, F. Jean-Alphonse, A. Karamitri, G. Guillaumet, P. Delagrange, R. M. Friedlander, J.-P. Vilardaga, F. Suzenet, R. Jockers, Design and validation of the first cell-impermeant melatonin receptor agonist. *Br. J. Pharmacol.* **174**, 2409–2421 (2017).
62. Y. Suofu, W. Li, F. G. Jean-Alphonse, J. Jia, N. K. Khattar, J. Li, S. V. Baranov, D. Leronni, A. C. Mihalik, Y. He, E. Cecon, V. L. Wehbi, J. Kim, B. E. Heath, O. V. Baranova, X. Wang, M. J. Gable, E. S. Kretz, G. Di Benedetto, T. R. Lezon, L. M. Ferrando, T. M. Larkin, M. Sullivan, S. Yablonska, J. Wang, M. B. Minnigh, G. Guillaumet, F. Suzenet, R. M. Richardson, S. M. Poloyac, D. B. Stolz, R. Jockers, P. A. Witt-Enderby, D. L. Carlisle, J.-P. Vilardaga, R. M. Friedlander, Dual role of mitochondria in producing melatonin and driving GPCR signaling to block cytochrome c release. *Proc. Natl. Acad. Sci. U.S.A.* **114**, E7997–E8006 (2017).
63. A. Busquets-Garcia, J. Bains, G. Marsicano, CB1 receptor signaling in the brain: Extracting specificity from ubiquity. *Neuropsychopharmacology.* **43**, 4–20 (2018).
64. P. M. Abadir, J. D. Walston, R. M. Carey, Subcellular characteristics of functional intracellular renin-angiotensin systems. *Peptides* **38**, 437–445 (2012).
65. T. Kimura, F. Murakami, Evidence that dendritic mitochondria negatively regulate dendritic branching in pyramidal neurons in the neocortex. *J. Neurosci.* **34**, 6938–6951 (2014).
66. R. Norkett, S. Modi, N. Birsa, T. A. Atkin, D. Ivankovic, M. Pathania, S. V. Trossbach, C. Korth, W. D. Hirst, J. T. Kittler, DISC1-dependent regulation of mitochondrial dynamics controls the morphogenesis of complex neuronal dendrites. *J. Biol. Chem.* **291**, 613–629 (2016).
67. R. Mancuso, A. Martínez-Muriana, T. Leiva, D. Gregorio, L. Ariza, M. Morell, J. Esteban-Pérez, A. García-Redondo, A. C. Calvo, G. Atencia-Cibreiro, G. Corfas, R. Osta, A. Bosch, X. Navarro, Neuregulin-1 promotes functional improvement by enhancing collateral sprouting in SOD1(G93A) ALS mice and after partial muscle denervation. *Neurobiol. Dis.* **95**, 168–178 (2016).
68. T. Gordon, J. Hegedus, S. L. Tam, Adaptive and maladaptive motor axonal sprouting in aging and motoneuron disease. *Neurol. Res.* **26**, 174–185 (2004).
69. I. Kushima, B. Aleksic, M. Nakatochi, T. Shimamura, T. Okada, Y. Uno, M. Morikawa, K. Ishizuka, T. Shiino, H. Kimura, Y. Arioka, A. Yoshimi, Y. Takasaki, Y. Yu, Y. Nakamura, M. Yamamoto, T. Iidaka, S. Iritani, T. Inada, N. Ogawa, E. Shishido, Y. Torii, N. Kawano, Y. Omura, T. Yoshikawa, T. Uchiyama, T. Yamamoto, M. Ikeda, R. Hashimoto, H. Yamamori, Y. Yasuda, T. Someya, Y. Watanabe, J. Egawa, A. Nunokawa, M. Itokawa, M. Arai, M. Miyashita, A. Kobori, M. Suzuki, T. Takahashi, M. Usami, M. Kodaira, K. Watanabe, T. Sasaki, H. Kuwabara, M. Tochigi, F. Nishimura, H. Yamasue, Y. Eriguchi, S. Benner, M. Kojima, W. Yassin, T. Munesue, S. Yokoyama, R. Kimura, Y. Funabiki, H. Kosaka, M. Ishitobi, T. Ohmori, S. Numata, T. Yoshikawa, T. Toyota, K. Yamakawa, T. Suzuki, Y. Inoue, K. Nakaoka, Y.-I. Goto, M. Inagaki, N. Hashimoto, I. Kusumi, S. Son, T. Murai, T. Ikegame, N. Okada, K. Kasai, S. Kunimoto, D. Mori, N. Iwata, N. Ozaki, Comparative analyses of copy-number variation in autism spectrum disorder and schizophrenia reveal etiological overlap and biological insights. *Cell Rep.* **24**, 2838–2856 (2018).
70. S. Sakaue, M. Kanai, Y. Tanigawa, J. Karjalainen, M. Kurki, S. Koshiba, A. Narita, T. Konuma, K. Yamamoto, M. Akiyama, K. Ishigaki, A. Suzuki, K. Suzuki, W. Obara, K. Yamaji, K. Takahashi, S. Asai, Y. Takahashi, T. Suzuki, N. Shinozaki, H. Yamaguchi, S. Minami, S. Murayama, K. Yoshimori, S. Nagayama, D. Obata, M. Higashiyama, A. Masumoto, Y. Koretsune, K. Ito, C. Terao, T. Yamauchi, I. Komuro, T. Kadowaki, G. Tamiya, M. Yamamoto, Y. Nakamura, M. Kubo, Y. Murakami, K. Yamamoto, Y. Kamatani, A. Palotie, M. A. Rivas, M. J. Daly, K. Matsuda, Y. Okada, A cross-population atlas of genetic associations for 220 human phenotypes. *Nat. Genet.* **53**, 1415–1424 (2021).
71. B. E. Cade, J. Lee, T. Sofer, H. Wang, M. Zhang, H. Chen, S. A. Gharib, D. J. Gottlieb, X. Guo, J. M. Lane, J. Liang, X. Lin, H. Mei, S. R. Patel, S. M. Purcell, R. Saxena, N. A. Shah, D. S. Evans, C. L. Hanis, D. R. Hillman, S. Mukherjee, L. J. Palmer, K. L. Stone, G. J. Tranah, NHLBI Trans-Omics for Precision Medicine (TOPMed) Consortium, G. R. Abecasis, E. A. Boerwinkle, A. Correa, L. A. Cupples, R. C. Kaplan, D. A. Nickerson, K. E. North, B. M. Psaty, J. I. Rotter, S. S. Rich, R. P. Tracy, R. S. Vasan, J. G. Wilson, X. Zhu, S. Redline, TOPMed Sleep Working Group, Whole-genome association analyses of sleep-disordered breathing phenotypes in the NHLBI TOPMed program. *Genome Med.* **13**, 136 (2021).
72. M. D. Shirley, H. Tang, C. J. Gallione, J. D. Baugher, L. P. Frelin, B. Cohen, P. E. North, D. A. Marchuk, A. M. Comi, J. Pevsner, Sturge–Weber syndrome and port-wine stains caused by somatic mutation in *GNAQ*. *N. Engl. J. Med.* **368**, 1971–1979 (2013).
73. E. A. Stahl, G. Breen, A. J. Forstner, A. McQuillin, S. Ripke, V. Trubetskoy, M. Mattheisen, Y. Wang, J. R. I. Coleman, H. A. Gaspar, C. A. de Leeuw, S. Steinberg, J. M. W. Pavlides, M. Trzaskowski, E. M. Byrne, T. H. Pers, P. A. Holmans, A. L. Richards, L. Abbott, E. Agerbo, H. Akil, D. Albani, N. Alliey-Rodriguez, T. D. Als, A. Anjorin, V. Antilla, S. Awasthi, J. A. Badner, M. Bækvad-Hansen, J. D. Barchas, N. Bass, M. Bauer, R. Belliveau, S. E. Bergen, C. B. Pedersen, E. Bøen, M. P. Boks, J. Boocock, M. Budde, W. Bunney, M. Burmeister, J. Bybjerg-Grauholm, W. Byerley, M. Casas, F. Cerrato, P. Cervantes, K. Chambert, A. W. Charney, D. Chen, C. Churchhouse, T. K. Clarke, W. Coryell, D. W. Craig, C. Cruceanu, D. Curtis, P. M. Czerski, A. M. Dale, S. de Jong, F. Degenhardt, J. Del-Favero, J. R. DePaulo, S. Djurovic, A. L. Dobbyn, A. Dumont, T. Elvsåshagen, V. Escott-Price, C. C. Fan, S. B. Fischer, M. Flickinger, T. M. Foroud, L. Forty, J. Frank, C. Fraser, N. B. Freimer, L. Frisén, K. Gade, D. Gage, J. Garnham, C. Giambartolomei, M. G. Pedersen, J. Goldstein, S. D. Gordon, K. Gordon-Smith, E. K. Green, M. J. Green, T. A. Greenwood, J. Grove, W. Guan, J. Guzman-Parra, M. L. Hamshere, M. Hautzinger, U. Heilbronner, S. Herms, M. Hipolito, P. Hoffmann, D. Holland, L. Huckins, S. Jamain, J. S. Johnson, A. Juréus, R. Kandaswamy, R. Karlsson, J. L. Kennedy, S. Kittel-Schneider, J. A. Knowles, M. Kogevinas, A. C. Koller, R. Kupka, C. Lavebratt, J. Lawrence, W. B. Lawson, M. Leber, P. H. Lee, S. E. Levy, J. Z. Li, C. Liu, S. Lucae, A. Maaser, D. J. MacIntyre, P. B. Mahon, W. Maier, L. Martinsson, S. McCarroll, P. McGuffin, M. G. McInnis, J. D. McKay, H. Medeiros, S. E. Medland, F. Meng, L. Milani, G. W. Montgomery, D. W. Morris, T. W. Mühleisen, N. Mullins, H. Nguyen, C. M. Nievergelt, A. N. Adolfsson, E. A. Nwulia, C. O'Donovan, L. M. O. Loohuis, A. P. S. Ori, L. Oruc, U. Ösby, R. H. Perlis, A. Perry, A. Pfennig, J. B. Potash, S. M. Purcell, E. J. Regeer, A. Reif, C. S. Reinbold, J. P. Rice, F. Rivas, M. Rivera, P. Roussos, D. M. Ruderfer, E. Ryu, C. Sánchez-Mora, A. F. Schatzberg, W. A. Scheftner, N. J. Schork, C. S. Weickert, T. Shehktman, P. D. Shilling, E. Sigurdsson, C. Slaney, O. B. Smeland, J. L. Sobell, C. S. Hansen, A. T. Spijker, D. S. Clair, M. Steffens, J. S. Strauss, F. Streit, J. Strohmaier, S. Szelinger, R. C. Thompson, T. E. Thorgeirsson, J. Treutlein, H. Vedder, W. Wang, S. J. Watson, T. W. Weickert, S. H. Witt, S. Xi, W. Xu, A. H. Young, P. Zandi, P. Zhang, S. Zöllner, R. Adolfsson, I. Agartz, M. Alda, L. Backlund, B. T. Baune, F. Bellivier, W. H. Berrettini, J. M. Biernacka, D. H. R. Blackwood, M. Boehnke, A. D. Børglum, A. Corvin, N. Craddock, M. J. Daly, U. Dannlowski, T. Esko, B. Etain, M. Frye, J. M. Fullerton, E. S. Gershon, M. Gill, F. Goes, M. Grigoroiu-Serbanescu, J. Hauser, D. M. Hougaard, C. M. Hultman, I. Jones, L. A. Jones, R. S. Kahn, G. Kirov, M. Landén, M. Leboyer, C. M. Lewis, Q. S. Li, J. Lissowska, N. G. Martin, F. Mayoral, S. L. McElroy, A. M. McIntosh, F. J. McMahon, I. Melle, A. Metspalu, P. B. Mitchell, G. Morken, O. Mors, P. B. Mortensen, B. Müller-Myhsok, R. M. Myers, B. M. Neale, V. Nimgaonkar, M. Nordentoft, M. M. Nöthen, M. C. O'Donovan, K. J. Oedegaard, M. J. Owen, S. A. Paciga, C. Pato, M. T. Pato, D. Posthuma, J. A. Ramos-Quiroga, M. Ribasés, M. Rietschel, G. A. Rouleau, M. Schalling,

P. R. Schofield, T. G. Schulze, A. Serretti, J. W. Smoller, H. Stefansson, K. Stefansson, E. Stordal, P. F. Sullivan, G. Turecki, A. E. Vaaler, E. Vieta, J. B. Vincent, T. Werge, J. I. Nurnberger, N. R. Wray, A. Di Florio, H. J. Edenberg, S. Cichon, R. A. Ophoff, L. J. Scott, O. A. Andreassen, J. Kelsoe, P. Sklar, Bipolar Disorder Working Group of the Psychiatric Genomics Consortium, Genome-wide association study identifies 30 loci associated with bipolar disorder. *Nat. Genet.* **51**, 793–803 (2019).

74. S. L. Pulit, C. Stoneman, A. P. Morris, A. R. Wood, C. A. Glastonbury, J. Tyrrell, L. Yengo, T. Ferreira, E. Marouli, Y. Ji, J. Yang, S. Jones, R. Beaumont, D. C. Croteau-Chonka, T. W. Winkler, A. T. Hattersley, R. J. F. Loos, J. N. Hirschhorn, P. M. Visscher, T. M. Frayling, H. Yaghootkar, C. M. Lindgren, Meta-analysis of genome-wide association studies for body fat distribution in 694 649 individuals of European ancestry. *Hum. Mol. Genet.* **28**, 166–174 (2019).
75. D. Grossmann, C. Berenguer-Escuder, M. E. Bellet, D. Scheibner, J. Bohler, F. Massart, D. Rapaport, A. Skupin, A. Fouquier D'Hérouël, M. Sharma, J. Ghelfi, A. Raković, P. Lichtner, P. Antony, E. Glaab, P. May, K. S. Dimmer, J. C. Fitzgerald, A. Grünewald, R. Krüger, Mutations in RHOT1 disrupt endoplasmic reticulum-mitochondria contact sites interfering with calcium homeostasis and mitochondrial dynamics in Parkinson's disease. *Antioxid. Redox Signal.* **31**, 1213–1234 (2019).
76. I. Iossifov, B. J. O'Roak, S. J. Sanders, M. Ronemus, N. Krumm, D. Levy, H. A. Stessman, K. T. Witherspoon, L. Vives, K. E. Patterson, J. D. Smith, B. Paeper, D. A. Nickerson, J. Dea, S. Dong, L. E. Gonzalez, J. D. Mandell, S. M. Mane, M. T. Murtha, C. A. Sullivan, M. F. Walker, Z. Waqar, L. Wei, A. J. Willsey, B. Yamrom, Y. H. Lee, E. Grabowska, E. Dalkic, Z. Wang, S. Marks, P. Andrews, A. Leotta, J. Kendall, I. Hakker, J. Rosenbaum, B. Ma, L. Rodgers, J. Troge, G. Narzisi, S. Yoon, M. C. Schatz, K. Ye, W. R. McCombie, J. Shendure, E. E. Eichler, M. W. State, M. Wigler, The contribution of de novo coding mutations to autism spectrum disorder. *Nature* **515**, 216–221 (2014).
77. J. J. Edwards, A. D. Rouillard, N. F. Fernandez, Z. Wang, A. Lachmann, S. S. Shankaran, B. W. Bisgrove, B. Demarest, N. Turan, D. Srivastava, D. Bernstein, J. Deanfield, A. Giardini, G. Porter, R. Kim, A. E. Roberts, J. W. Newburger, E. Goldmuntz, M. Brueckner, R. P. Lifton, C. E. Seidman, W. K. Chung, M. Tristani-Firouzi, H. J. Yost, A. Ma'ayan, B. D. Gelb, Systems analysis implicates WAVE2 complex in the pathogenesis of developmental left-sided obstructive heart defects. *JACC Basic to Transl. Sci.* **5**, 376–386 (2020).
78. Q. Fan, V. J. M. Verhoeven, R. Wojciechowski, V. A. Barathi, P. G. Hysi, J. A. Guggenheim, R. Hohn, V. Vitart, A. P. Khawaja, K. Yamashiro, S. M. Hosseini, T. Lehtimaki, Y. Lu, T. Haller, J. Xie, C. Delcourt, M. Pirastu, J. Wedenoja, P. Gharahkhani, C. Venturini, M. Miyake, A. W. Hewitt, X. Guo, J. Mazur, J. E. Huffman, K. M. Williams, O. Polasek, H. Campbell, I. Rudan, Z. Vatavuk, J. F. Wilson, P. K. Joshi, G. McMahon, B. St Pourcain, D. M. Evans, C. L. Simpson, T. H. Schwantes-An, R. P. Igo, A. Mirshahi, A. Cougnard-Gregoire, C. Bellenguez, M. Blettner, O. Raitakari, M. Kahonen, I. Seppala, T. Zeller, T. Meitinger, J. S. Ried, C. Gieger, L. Portas, E. M. Van Leeuwen, N. Amin, A. G. Uitterlinden, F. Rivadeneira, A. Hofman, J. R. Vingerling, Y. X. Wang, X. Wang, E. Tai-Hui Boh, M. K. Ikram, C. Sabanayagam, P. Gupta, V. Tan, L. Zhou, C. E. H. Ho, W. Lim, R. W. Beuerman, R. Siantar, E. S. Tai, E. Vithana, E. Mihailov, C. C. Khor, C. Hayward, R. N. Luben, P. J. Foster, B. E. K. Klein, R. Klein, H. S. Wong, P. Mitchell, A. Metspalu, T. Aung, T. L. Young, M. He, O. Parssinen, C. M. Van Duijn, J. Jin Wang, C. Williams, J. B. Jonas, Y. Y. Teo, D. A. MacKey, K. Oexle, N. Yoshimura, A. D. Paterson, N. Pfeiffer, T. Y. Wong, P. N. Baird, D. Stambolian, J. E. B. Wilson, C. Y. Cheng, C. J. Hammond, C. C. W. Klaver, S. M. Saw, J. S. Rahi, J. F. Korobelnik, J. P. Kemp, N. J. Timpson, G. D. Smith, J. E. Craig, K. P. Burdon, R. D. Fogarty, S. K. Iyengar, E. Chew, S. Janmahasatian, N. G. Martin, S. MacGregor, L. Xu, M. Schache, V. Nangia, S. Panda-Jonas, A. F. Wright, J. R. Fondran, J. H. Lass, S. Feng, J. H. Zhao, K. T. Khaw, N. J. Wareham, T. Rantanen, J. Kaprio, C. P. Pang, L. J. Chen, P. O. Tam, V. Jhanji, A. L. Young, A. Doring, L. J. Raffel, M. F. Cotch, X. Li, S. P. Yip, M. K. H. Yap, G. Biino, S. Vaccargiu, M. Fossarello, B. Fleck, S. Yazar, J. W. L. Tideman, M. Tedja, M. M. Deangelis, M. Morrison, L. Farrer, X. Zhou, W. Chen, N. Mizuki, A. Meguro, K. M. Makela, Meta-analysis of gene-environment-wide association scans accounting for education level identifies additional loci for refractive error. *Nat. Commun.* **7**, 11008 (2016).
79. J. Hällfors, T. Palviainen, I. Surakka, R. Gupta, J. Buchwald, A. Raevuori, S. Ripatti, T. Korhonen, P. Jousilahti, P. A. F. Madden, J. Kaprio, A. Loukola, Genome-wide association study in Finnish twins highlights the connection between nicotine addiction and neurotrophin signaling pathway. *Addict. Biol.* **24**, 549–561 (2019).
80. M. Liu, Y. Jiang, R. Wedow, Y. Li, D. M. Brazel, F. Chen, G. Datta, J. Davila-Velderrain, D. McGuire, C. Tian, X. Zhan, 23andMe Research Team, HUNT All-In Psychiatry, H. Choquet, A. R. Docherty, J. D. Faul, J. R. Foerster, L. G. Fritsche, M. E. Gabrielsen, S. D. Gordon, J. Haessler, J.-J. Hottenga, H. Huang, S.-K. Jang, P. R. Jansen, Y. Ling, R. Mägi, N. Matoba, G. McMahon, A. Mulas, V. Orrù, T. Palviainen, A. Pandit, G. W. Reginsson, A. H. Skogholt, J. A. Smith, A. E. Taylor, C. Turman, G. Willemsen, H. Young, K. A. Young, G. J. M. Zajac, W. Zhao, W. Zhou, G. Bjornsdottir, J. D. Boardman, M. Boehnke, D. I. Boomsma, C. Chen, F. Cucca, G. E. Davies, C. B. Eaton, M. A. Ehringer, T. Esko, E. Fiorillo, N. A. Gillespie, D. F. Gudbjartsson, T. Haller, K. M. Harris, A. C. Heath, J. K. Hewitt, I. B. Hickie, J. E. Hokanson, C. J. Hopfer, D. J. Hunter, W. G. Iacono, E. O. Johnson, Y. Kamatani, S. L. R. Kardia, M. C. Keller, M. Kellis, C. Kooperberg, P. Kraft, K. S. Krauter, M. Laakso, P. A. Lind, A. Loukola, S. M. Lutz, P. A. F. Madden, N. G. Martin, M. McGue, M. B. McQueen, S. E. Medland, A. Metspalu, K. L. Mohlke, J. B. Nielsen, Y. Okada, U. Peters, T. J. C. Polderman, D. Posthuma, A. P. Reiner, J. P. Rice, E. Rimm, R. J. Rose, V. Runarsdottir, M. C. Stallings, A. Stančáková, H. Stefansson, K. K. Thai, H. A. Tindle, T. Tyrfingsson, T. L. Wall, D. R. Weir, C. Weisner, J. B. Whitfield, B. S. Winsvold, J. Yin, L. Zuccolo, L. J. Bierut, K. Hveem, J. J. Lee, M. R. Munafo, N. L. Saccone, C. J. Willer, M. C. Cornelis, S. P. David, D. Hinds, E. Jorgenson, J. Kaprio, J. A. Stitzel, K. Stefansson, T. E. Thorgeirsson, G. Abecasis, D. J. Liu, S. Vrieze, Association studies of up to 1.2 million individuals yield new insights into the genetic etiology of tobacco and alcohol use. *Nat. Genet.* **51**, 237–244 (2019).
81. N. Verweij, J. W. Benjamins, M. P. Morley, Y. J. van de Vegte, A. Teumer, T. Trenkwalder, W. Reinhard, T. P. Cappola, P. van der Harst, The genetic makeup of the electrocardiogram. *Cell Syst.* **11**, 229–238.e5 (2020).
82. A. Grupe, R. Abraham, Y. Li, C. Rowland, P. Hollingworth, A. Morgan, L. Jehu, R. Segurado, D. Stone, E. Schadt, M. Karnoub, P. Nowotny, K. Tacey, J. Catanese, J. Sninsky, C. Brayne, D. Rubinsztein, M. Gill, B. Lawlor, S. Lovestone, P. Holmans, M. O'Donovan, J. C. Morris, L. Thal, A. Goate, M. J. Owen, J. Williams, Evidence for novel susceptibility genes for late-onset Alzheimer's disease from a genome-wide association study of putative functional variants. *Hum. Mol. Genet.* **16**, 865–873 (2007).
83. J. Sun, H. R. Kranzler, J. Gelernter, J. Bi, A genome-wide association study of cocaine use disorder accounting for phenotypic heterogeneity and gene–environment interaction. *J. Psychiatry Neurosci.* **45**, 34–44 (2020).
84. N. Brandes, N. Linial, M. Linial, Genetic association studies of alterations in protein function expose recessive effects on cancer predisposition. *Sci. Rep.* **11**, 14901 (2021).
85. J. Liu, Y. Zhou, S. Liu, X. Song, X. Z. Yang, Y. Fan, W. Chen, Z. C. Akdemir, Z. Yan, Y. Zuo, R. Du, Z. Liu, B. Yuan, S. Zhao, G. Liu, Y. Chen, Y. Zhao, M. Lin, Q. Zhu, Y. Niu, P. Liu, S. Ikegawa, Y. Q. Song, J. E. Posey, G. Qiu, F. Zhang, Z. Wu, J. R. Lupski, N. Wu, The coexistence of copy number variations (CNVs) and single nucleotide polymorphisms (SNPs) at a locus can result in distorted calculations of the significance in associating SNPs to disease. *Hum. Genet.* **137**, 553–567 (2018).
86. A. G. Comuzzie, S. A. Cole, S. L. Laston, V. S. Voruganti, K. Haack, R. A. Gibbs, N. F. Butte, Novel genetic loci identified for the pathophysiology of childhood obesity in the Hispanic population. *PLOS ONE* **7**, e51954 (2012).
87. R. Karlsson Linnér, T. T. Mallard, P. B. Barr, S. Sanchez-Roige, J. W. Madole, M. N. Driver, H. E. Poore, R. de Vlaming, A. D. Grotzinger, J. J. Tielbeek, E. C. Johnson, M. Liu, S. B. Rosenthal, T. Ideker, H. Zhou, R. L. Kember, J. A. Pasman, K. J. H. Verweij, D. J. Liu, S. Vrieze, COGA Collaborators, H. R. Kranzler, J. Gelernter, K. M. Harris, E. M. Tucker-Drob, I. D. Waldman, A. A. Palmer, K. P. Harden, P. D. Koellinger, D. M. Dick, Multivariate analysis of 1.5 million people identifies genetic associations with traits related to self-regulation and addiction. *Nat. Neurosci.* **24**, 1367–1376 (2021).
88. V. A. Kulkarni, B. L. Firestein, The dendritic tree and brain disorders. *Mol. Cell. Neurosci.* **50**, 10–20 (2012).
89. J. Grutzendler, K. Helmin, J. Tsai, W.-B. Gan, Various dendritic abnormalities are associated with fibrillar amyloid deposits in Alzheimer's disease. *Ann. N. Y. Acad. Sci.* **1097**, 30–39 (2007).
90. E. Shimobayashi, J. P. Kapfhammer, Calcium signaling, PKC gamma, IP3R1 and CAR8 link spinocerebellar ataxias and purkinje cell dendritic development. *Curr. Neuropharmacol.* **16**, 151–159 (2018).
91. M. Liesa, B. Borda-d'Água, G. Medina-Gómez, C. J. Lelliott, J. C. Paz, M. Rojo, M. Palacín, A. Vidal-Puig, A. Zorzano, Mitochondrial fusion is increased by the nuclear coactivator PGC-1β. *PLOS ONE* **3**, e3613 (2008).
92. A. M. Aragay, A. Katz, M. I. Simon, The G alpha q and G alpha 11 proteins couple the thyrotropin-releasing hormone receptor to phospholipase C in GH3 rat pituitary cells. *J. Biol. Chem.* **267**, 24983–24988 (1992).
93. B. B. Johansson, L. Minsaas, A. M. Aragay, Proteasome involvement in the degradation of the G_q family of G_α subunits. *FEBS J.* **272**, 5365–5377 (2005).
94. H. Schägger, [12] Native electrophoresis for isolation of mitochondrial oxidative phosphorylation protein complexes. *Methods Enzymol.* **260**, 190–202 (1995).
95. X. Wang, D. Winter, G. Ashrafi, J. Schlehe, Y. L. Wong, D. Selkoe, S. Rice, J. Steen, M. J. LaVoie, T. L. Schwarz, PINK1 and parkin target miro for phosphorylation and degradation to arrest mitochondrial motility. *Cell* **147**, 893–906 (2011).
96. K. Deinhardt, S. Salinas, C. Verastegui, R. Watson, D. Worth, S. Hanrahan, C. Bucci, G. Schiavo, Rab5 and Rab7 control endocytic sorting along the axonal retrograde transport pathway. *Neuron* **52**, 293–305 (2006).
97. T. Uemura, H. Takamatsu, T. Kawasaki, M. Taniguchi, E. Yamamoto, Y. Tomura, W. Uchida, K. Miyata, Effect of YM-254890, a specific $G\alpha_q$/11inhibitor, on experimental peripheral arterial disease in rats. *Eur. J. Pharmacol.* **536**, 154–161 (2006).
98. B. N. Armbruster, X. Li, M. H. Pausch, S. Herlitze, B. L. Roth, Evolving the lock to fit the key to create a family of G protein-coupled receptors potently activated by an inert ligand. *Proc. Natl. Acad. Sci.* **104**, 5163–5168 (2007).
99. R. D. Beech, M. A. Cleary, H. B. Treloar, A. J. Eisch, A. V. Harrist, W. Zhong, C. A. Greer, R. S. Duman, M. R. Picciotto, Nestin promoter/enhancer directs transgene expression to precursors of adult generated periglomerular neurons. *J. Comp. Neurol.* **475**, 128–141 (2004).

100. S. J. Guyenet, S. A. Furrer, V. M. Damian, T. D. Baughan, A. R. La Spada, G. A. Garden, A simple composite phenotype scoring system for evaluating mouse models of cerebellar ataxia. *J. Vis. Exp.* **39**, 1787 (2010).
101. B. F. El-Khodor, N. Edgar, A. Chen, M. L. Winberg, C. Joyce, D. Brunner, M. Suárez-Fariñas, M. P. Heyes, Identification of a battery of tests for drug candidate evaluation in the SMNΔ7 neonate model of spinal muscular atrophy. *Exp. Neurol.* **212**, 29–43 (2008).
102. G. Paxinos, K. B. J. Franklin, *The Mouse Brain in Stereotaxic Coordinates* (Academic Press, 1997).
103. R. Mancuso, E. Santos-Nogueira, R. Osta, X. Navarro, Electrophysiological analysis of a murine model of motoneuron disease. *Clin. Neurophysiol.* **122**, 1660–1670 (2011).

Acknowledgments: We thank S. E. Rubio for discussion and critical reading of the manuscript, the MBU microscopy core facility (MRC, UK) for assistance with the super-resolution imaging, and B. Bouazza (Charité–Universitätsmedizin Berlin, Germany) for help with some experiments. **Funding:** This work was funded by the Ministerio de Ciencia e Innovación (grants BFU2017-83379-R to A.M.A., SAF2016-76340R PID2019-106764RB-C21 and PID2022-138105OB-C21 to E.S., SAF2015-65633-R and RTI2018-099357-B-I00 to J.A.E., RTI2018-096386-B-I00 to X.N., EQC2018-004541-P support to E.R., Severo Ochoa Excellence program to J.A.E., and María de Maeztu Excellence program to E.S.), CSIC13-4E-2065 to the Molecular Imaging Platform, and Instituto de Salud Carlos III (CIBERNED to E.S., C.A., X.N. and A.L.d.M.; CIBERER to G.M.; CIBERFES to J.A.E.; grant PI18/01066 to A.L.d.M.; and a collaborative CIBERNED project to E.S. and A.L.d.M.). J.A.E. is supported by the HFSP (RGP0016/2018) and the Pro CNIC Foundation. A.L.d.M. is supported by EiTB Maratoia, grant number BIO17/ND/023, and by Osasun Saila, Eusko Jaurlaritzako, grant number 2015111122. F.J.G.-B. was supported by Roche Stop Fuga de Cerebros (BIO19/ROCHE/017/BD). I.I.-V. was supported by an FI fellowship from AGAUR.
Author contributions: I.I.-V., S.M., and Y.M. performed or participated in most experiments. A.P. and M.H.-L. measured dendritic parameters. C.B., J.R., and J.A.E. conducted the proteome analysis and performed biochemical analyses of Alex3 and $G\alpha_q$. S.M. and Y.M. generated the Alex3 CKO model. F.U. analyzed the spinal cord. C.A., R.D.C.-T., and E.V. performed biochemical analyses in KO mice. E.R. provided support with live imaging acquisition and analysis. X.N. and J.D.V. performed the in vivo electrophysiology experiments. F.J.G.-B. and A.L.d.M. performed the neuromuscular synapse analysis. G.M. performed genetic analysis. I.I.-V., S.M., Y.M., A.M.A., and E.S. wrote the draft of the manuscript. All authors read and corrected the manuscript. Y.M., A.M.A. and E.S. wrote the final manuscript. A.M.A. and E.S. conceived and supervised the study.
Competing interests: The authors declare that they have no competing interests. **Data and materials availability:** The mitoproteomics MS data have been deposited in ProteomeXchange under the project PXD046668. All other data needed to evaluate the conclusions in the paper are present in the paper and/or the Supplementary Materials. Plasmids are available from A.M.A. Alex3 CKO mice are freely available from E.S.

Submitted 17 March 2022
Resubmitted 6 June 2023
Accepted 16 January 2024
Published 6 February 2024
10.1126/scisignal.abq1007